Geochimica et Cosmochimica Acta xxx (xxxx) xxx

Contents lists available at ScienceDirect

Geochimica et Cosmochimica Acta

journal homepage: www.elsevier.com/locate/gca

Trace element partitioning between apatite and silicate melts: Effects of major element composition, temperature, and oxygen fugacity, and implications for the volatile element budget of the lunar magma ocean

Dian Ji *, Nicholas Dygert

Department of Earth and Planetary Sciences, University of Tennessee, Knoxville, TN 37996, USA

ARTICLE INFO

Associate editor: Yuan Li

Keywords:
Trace element partitioning
Apatite
Oxybarometer
KREEP basalt

ABSTRACT

Apatite, as an accessory phase in igneous and metamorphic rocks, has important petrological significance due to its capacity to accommodate appreciable amounts of many trace elements in its mineral structure. To better constrain trace element partitioning between apatite and silicate melts, we conducted experiments that produced apatites approaching fluorapatite (FlAp), hydroxylapatite (OHAp) and chlorapatite (ClAp) endmembers separately at 1050 and 1100 °C, 1 GPa pressure, under oxygen fugacity (fO_2) about one log unit below iron-wüstite buffer to four log unit above fayalite-magnetite-quartz buffer. We report the results of 12 experiments which demonstrate that ClAp exhibits lower trace element partition coefficients compared with FlAp and OHAp, especially for Rare Earth Elements (REEs) under all run conditions explored, suggesting trace element partitioning is sensitive to anion site occupancy. Divalent cations are less sensitive to anion occupancy. Positive Eu partitioning anomalies (DEu/DEu*, where Eu is the chondrite normalized abundance and Eu* is the interpolated value from neighboring elements ordered by atomic number) are observed in ClAp experiments under relatively low fO_2s, whereas negative Eu anomalies are exhibited by FlAp and OHAp under the same fO_2 conditions. We infer that anionic occupancies have a direct impact on the substitution mechanisms of trace elements in apatite, thereby influencing their partition coefficients. Beyond the anions, correlations of apatite compositional components (X_{Ca}, X_{Na}, X_P and X_{Si}) with partition coefficients suggest they exert crystal chemical controls on trace element partitioning. Based on these observations, we developed parameterized lattice strain models to predict the partitioning of divalent and trivalent elements as a function of temperature and apatite composition, and an fO_2-dependent apatite-melt Eu partitioning model and oxybarometer. We further developed a Eu in apatite-plagioclase oxybarometer that enables us to calculate the fO_2 of apatite and plagioclase-bearing magmatic and subsolidus systems, and evaluated the influence of subsolidus reequilibration on the new oxybarometer. Applied to one of our experiments, winonaite HaH193, and samples from Sept Iles layered intrusion, the oxybarometer recovers their anticipated fO_2s, ranging from about two log units below the iron-wüstite buffer to the fayalite-magnetite-quartz buffer. Using the new REE and fO_2-dependent Eu partitioning models, we constrained the petrogenesis of lunar KREEP basalt and estimated the relative volatile content in the late lunar magma ocean (LMO) cumulates. The model suggests a relative depletion of Cl in the LMO cumulates, consistent with Cl isotopic analyses and volatile abundance measurements in previous work, suggesting that differential loss of volatiles occurred before or during the late-stage evolution of the LMO.

1. Introduction

Apatite [$Ca_5(PO_4)_3(OH, F, Cl)$] is an omnipresent accessory mineral in different kinds of rocks on Earth as well as other bodies in the Solar System (e.g., McCubbin and Jones, 2015). Although representing a small proportion of the rock and acting as a late-crystallizing mineral, apatite can harbor an abundance of Rare Earth Elements (REEs) and other trace elements in magmatic systems because of the high partition coefficients (*Ds*) of these elements, which often approach or exceed unity (Gromet and Silver, 1983).

Some apatites, as well as whitlockites [$Ca_3(PO_4)_2$], have also been discovered in returned Apollo samples (e.g., Shervais et al., 1984;

* Corresponding author at: Department of Earth, Environmental and Planetary Sciences, Rice University, 6100 Main Street, MS 126, Houston, TX 77005, USA.
E-mail address: dj56@rice.edu (D. Ji).

https://doi.org/10.1016/j.gca.2023.11.004
Received 20 July 2023; Accepted 4 November 2023
Available online 7 November 2023
0016-7037/© 2023 Elsevier Ltd. All rights reserved.

Tartèse et al., 2014; Potts et al., 2018). Apatite also precipitates in the late stages of lunar magma ocean (LMO) crystallization experiments (e.g., Rapp and Draper, 2018, Schmidt and Kraettli, 2022). Since it has much higher partition coefficients for REEs than major minerals, apatite largely determines bulk elemental partitioning and affects elemental concentrations in major minerals during the solidification of a magma body (e.g., the LMO), as well as subsequent geological events (e.g., partial melting, subsolidus reequilibration). Therefore, developing predictive elemental partitioning models for trace elements between apatite and silicate melts is of importance to help us evaluate related fractionation processes.

Elemental partitioning between apatite and melt is complicated due to the uncertainty of the REE occupancy in the apatite. Because of the similarity of ion radius and valence state, divalent and trivalent cations often substitute for Ca^{2+} ions in mineral structures. In apatite, forty percent of the Ca atoms occupy a larger nine-fold coordinated lattice site (Ca1 site), while the rest enter a seven-fold coordinated site (Ca2 site), surrounding an anion-hosting X-site, which is usually occupied by F, OH, or Cl in naturally occurring apatites (Fig. S1). There is controversy in the literature over whether REEs tend to occupy the Ca1 site (Urusov and Khudolozhkin, 1974), Ca2 site (Borisov and Klevtsova, 1963), or have no occupancy preference (Cockbain and Smith, 1967). More recent studies suggest that for three endmembers of apatite, i.e., fluorapatite, hydroxylapatite, and chlorapatite (FlAp, OHAp, and ClAp), REE substitution mechanisms are related to the occupancy of X-site, as anions with different radii can modify the elastic properties of the Ca sites and the overall structure of apatite (e.g., Fleet and Pan, 1997; Fleet et al., 2000a; Fleet et al., 2000b). Site substitutions for divalent cations are also uncertain, and the site preference for each cation may be different (e.g., Pan and Fleet, 2002 and references therein). Previous studies reveal that temperature (Li and Hermann, 2017), as well as the polymerization of the melt (Prowatke and Klemme, 2006; Watson and Green, 1981), have large impacts on REE partition coefficients. However, because of a lack of data, relationships between the X-site occupancy (F, OH, Cl) and the REE partitioning behavior could not previously be quantified. In addition, a negative Eu anomaly (Eu/Eu*, where Eu is the chondrite normalized abundance and Eu* is the interpolated value from neighboring elements on a REE diagram) is generally reported in natural apatites (e.g., Chen et al., 2016), but the dependence of Eu partitioning on fO_2 was largely unknown and thus merited further exploration.

In this study, we experimentally determine trace element partition coefficients between apatite and silicate melt. We develop temperature and composition-dependent predictive partitioning models for divalent and trivalent elements, and quantify the effects of variations in composition and oxygen fugacity on Eu anomalies in apatite. We present a new Eu in apatite-plagioclase oxybarometer and explore the kinetic fractionation of trivalent and divalent Eu during subsolidus reequilibration, and evaluate its effect on the oxybarometer. Finally, we apply our predictive partitioning models to the LMO solidification and estimate the relative volatile abundance in the late-stage LMO cumulates.

2. Methods

2.1. Starting materials

Three different starting materials were used in our experiments with the same bulk composition with the exception of the anionic component. The bulk composition of major element cations is from the liquid in a LMO solidification experiment by Rapp and Draper (2018), where the melt composition is in equilibrium with apatite after the solidification percentage reaches 97 % (their L-GM25 experiment). Starting materials were prepared by grinding reagent-grade oxide and carbonate powders into three separate homogeneous mixtures. A mixture of REEs, HFSEs, and actinides, prepared from natural mineral sources was added into the starting compositions as a dopant at a mass ratio of ~ 1.5:100. After decarbonating the mixtures in an 850 ℃ furnace overnight, we preconditioned each mixture in a 900 ℃ H_2-CO_2 gas mixing furnace for 4 h according to the target fO_2s of three assembly types that utilize different metals to affect the experimental fO_2 (C-lined Mo, C-lined Mo and Cr, and Pt jacketed Re-ReO_2). Synthetic $Ca_5(PO_4)_3OH$, CaF_2 and NaCl were then added into the mixtures and mechanically dry mixed to keep the same molar percentage of F, Cl, OH, as well as other cations in each starting material. The compositions were stored in a vacuum furnace at 200 ℃ prior to running.

In order to obtain representative analyses of the experimental starting materials, three quenching experiments were conducted in which each of the starting components was placed in a separate graphite-lined Mo capsule and heated to 1250 °C at a ramp rate of 70 ℃ per minute under 1 GPa in the piston-cylinder apparatus, and the target temperature was maintained for one hour prior to quenching. Because of the high concentrations of FeO in our initial compositions, the three powders we utilized are those designed and preconditioned for experiments with relatively high fO_2 in order to avoid the formation of Fe metals during heating (more details about experimental procedures are reported in Sections 2.2 and 2.3). The experimental products contain only quenched glass, and the results of EMP analysis are reported in Table 1.

2.2. Capsules and preconditioning procedure

Piston cylinder experiments utilized graphite-lined molybdenum or platinum capsules, depending on the target fO_2. Experiments with Pt capsules targeted high fO_2 conditions. To mitigate reaction of the Pt capsules with the starting material during experiments, we preconditioned platinum capsules by crimping and welding one end shut, then placing the capsule in a platinum crucible in a bath of our starting materials (same as the composition in Table 1 but without phosphorous and volatile elements F, Cl, and OH), so that both the inner and outer wall of the capsule were surrounded. Preconditioning runs were conducted in a Deltech gas mixing furnace at 1200 ℃ for 24 h, in an H_2-CO_2 mixture approximating the intended fO_2 of the subsequent piston cylinder run. After removal from the Deltech furnace, the basalt glass within and around the capsules was dissolved in a mixture of nitric and hydrofluoric acid.

The series of experiments that utilized Mo capsules with graphite liners targeted fO_2s near the iron-wüstite buffer (e.g., Dygert et al., 2014; Fabbrizio et al., 2021). To target even more reducing conditions, a similar assembly design was used, but containing a layer of Cr metal powder isolated from the experimental powders and outer capsule by

Table 1
Major element compositions of the three starting materials utilized in this study.

	OHAp-M[a]		FlAp-M		ClAp-M	
n.o.a.[b]	(20)	σ	(29)	σ	(20)	σ
SiO_2	37.62	0.35	37.29	0.30	37.69	0.36
TiO_2	3.40	0.05	3.54	0.05	3.54	0.05
Al_2O_3	5.78	0.47	5.63	0.10	5.76	0.08
FeO	30.82	0.27	31.86	0.32	31.03	0.33
MnO	0.81	0.02	0.79	0.02	0.71	0.02
MgO	0.96	0.02	0.99	0.02	0.96	0.02
CaO	11.10	0.10	10.93	0.11	10.90	0.12
Na_2O	0.83	0.04	0.82	0.03	0.64	0.08
K_2O	0.19	0.01	0.25	0.01	0.20	0.01
P_2O_5	4.22	0.07	4.25	0.05	4.34	0.07
F	0.00	–	0.20	0.01	0.00	–
Cl	0.03	0.01	0.03	0.01	0.78	0.02
Spec[c]	1.50	–	1.50	–	1.50	–
Tot.	97.26		98.08		98.05	

[a] OH concentration cannot be directly analyzed by EMP, by calculation, the bulk OH abundance is about 0.28 wt%.
[b] Numbers of EMP analyses.
[c] The approximate sum of REEs, HFSEs, and actinides intentionally added to the starting materials.

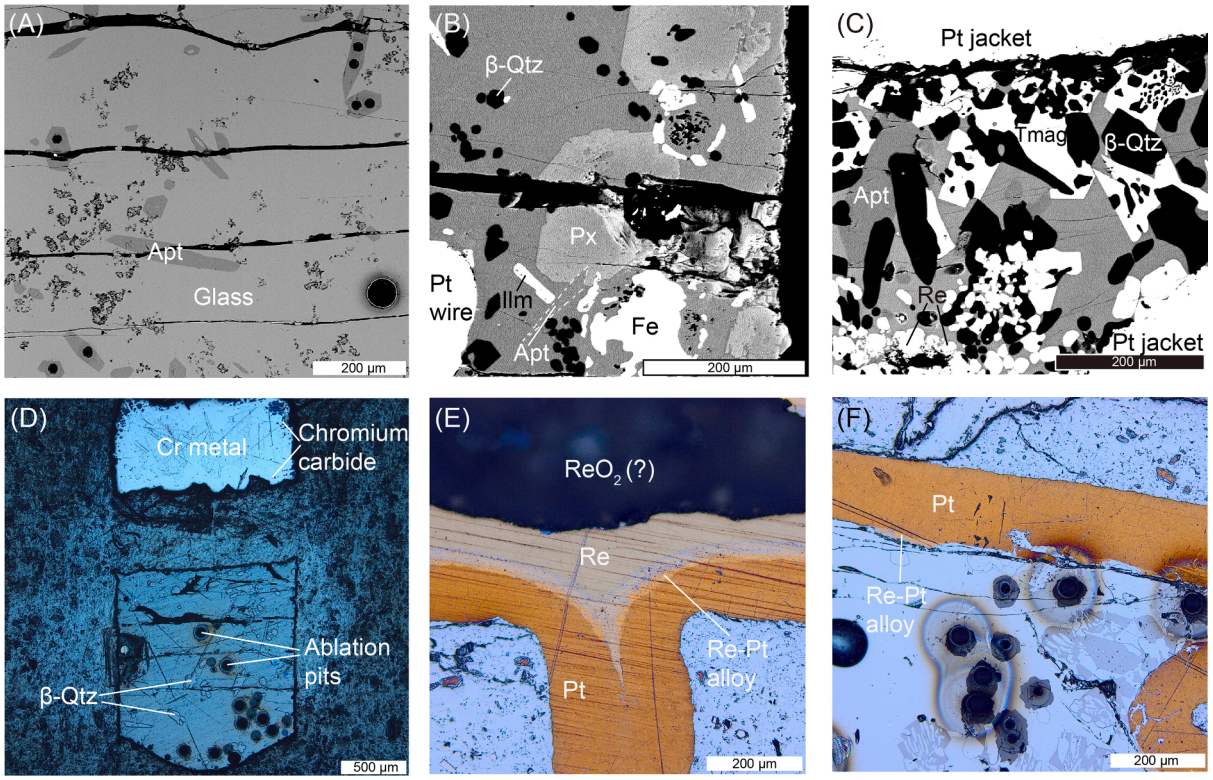

Fig. 1. Representative backscatter electron (A-C) and reflected light (D-F) images of experimental run products. (A) OHAp-6, (B) FlAp-9, (C) OHAp-7, (D) OHAp-5, (E) the bottom and (F) the top of experiment ClAp-5. There are some Re stains on the surface of the experiment (C), which may have been emplaced during polishing. At the bottom of the experiment (E), there is still some Re metal left, while Re also alloyed with Pt capsule. The location where ReO_2 was originally placed is now a void; the ReO_2 powder could be lost during polishing. At the top of the experiment shown in (F), Re-Pt alloy can still be seen in a few locations; we intentionally avoided these areas when measuring Fe alloyed concentrations.

layers of graphite. To monitor fO_2 in a subset of the graphite-lined Mo and graphite-lined Mo with Cr experiments, we placed preconditioned platinum wire in the experimental powders (Fig. 1B), prepared using the same method as employed for conditioning the platinum capsules, but at a higher H_2-CO_2 conditioning ratio appropriate to the target run condition.

2.3. Run procedure and conditions

Twelve high-temperature, high-pressure experiments were conducted at the University of Tennessee using a 19.1 mm end-loaded piston-cylinder apparatus. The assemblies utilized concentric shells of NaCl (as the pressure medium), an inner Pyrex® sleeve, and crushable MgO parts within a graphite furnace. In the oxidized experiments utilizing Pt capsules, a layer of Re and ReO_2 was placed beneath the starting materials inside the preconditioned Pt capsules, with the ReO_2 in direct contact with the experimental powders. After loading experimental powders, the open capsule ends were crimped and welded shut. Experimental fO_2s were monitored by measuring the composition of the platinum-iron alloy after the experiments. The method for calculating fO_2 from the composition of the alloy is reported in Section 3.4. All experiments were heated to 1200 °C at a ramp rate of 70 °C per minute, fused for one hour, and then cooled to the run temperature at a rate of 0.1 °C per minute, with pressure maintained at 1 GPa using a computerized pressure holding system. Temperatures were monitored using calibrated $W_{95}Re_5$ – $W_{75}Re_{25}$ thermocouples and run durations were 48 to 76 h after reaching the target conditions (Table 2).

2.4. Analytical techniques

We analyzed the major and trace element concentrations of plagioclase in OHAP-1, as well as apatite and quenched glass in all experiments. Major element compositions were characterized using a Cameca SX-100 electron microprobe (EMP) at the University of Tennessee. We utilized a 5 μm spot size and 10nA current to analyze apatite and quenched glass at an accelerating voltage of 15 keV. Analytical standards used are fluorapatite and HgCl for apatite phosphorus and X-site occupancy, with mass deficit used to characterize the OHAp component. Other standards applied are diopside (Si and Ca), TiO_2 (Ti), hematite (Fe), spessartine garnet (Mn), olivine (Mg), spinel (Al), albite (Na), orthoclase (K), as well as Pt, Cr, and Re metal. Background and peak counting times for the major elements were typically 20–30 s, and ZAF corrections were applied using the Cameca PAP procedure.

Trace element concentrations in minerals were determined using a New Wave UP193FX laser unit with a dual-volume sample chamber coupled to an Agilent 7500ce Quadrupole Inductively Coupled Plasma Mass Spectrometer (ICP-MS) at the University of Texas, Austin. Most apatites were ablated with a 20 μm spot and a few small apatites were analyzed using a 15 μm spot. For glass and plagioclase, we chose 30, 40 and 60 μm diameter spots according to the size of the phase; care was taken to avoid phase mixing. Analyses were conducted with a laser fluence of 2.5 J/cm^2 at a frequency of 20 Hz. Data were calibrated using CaO for apatite and SiO_2 for glass and plagioclase as a reference analyte from EMP analyses. The primary trace element standard material for apatite is Apatite-NP-B01 (myStandards GmbH), secondary standard materials for the apatite analyses are BCR-2G, NIST glass SRM 610 and 612. The primary reference analyte for glass and plagioclase is NIST glass SRM 610; and secondary standard materials are BCR-2G and NIST

Table 2
Experimental run conditions.

Experiment	Run pressure (GPa)	Run temperature (℃)	Ramp (℃/min)	Duration at target condition (h)	Starting material	Capsule type	Run Product[c]
FlAp-9[a]	1	1050	0.1	71	FlAp-M	C-lined Mo	Apt + β-Qtz + Ilm + Px + Fe + Melt
OHAp-1	1	1050	0.1	64	OHAp-M	C-lined Mo	Apt + β-Qtz + Ilm + Px + Fe + Melt
ClAp-1	1	1050	0.1	64	ClAp-M	C-lined Mo	Apt + β-Qtz + Ilm + Px + Fe + Melt
FlAp-1	1	1100	0.1	48	FlAp-M	C-lined Mo	Apt + β-Qtz + Fe + Melt
OHAp-6	1	1100	0.1	73	OHAp-M	C-lined Mo	Apt + β-Qtz + Fe + Melt
ClAp-2	1	1100	0.1	72	ClAp-M	C-lined Mo	Apt + β-Qtz + Fe + Melt
FlAp-8[a]	1	1100	0.1	76	FlAp-M	C-lined Cr & Mo	Apt + β-Qtz + Ttn + Fe + Melt
OHAp-5	1	1100	0.1	76	OHAp-M	C-lined Cr & Mo	Apt + β-Qtz + Fe + Melt
ClAp-3	1	1100	0.1	73	ClAp-M	C-lined Cr & Mo	Apt + β-Qtz + Plag + Fe + Melt
FlAp-7[a]	1	1100	0.1	54	FlAp-M	Pt-Re-ReO_2	Apt + β-Qtz + Tmag + Melt
OHAp-7[a b]	1	1100	0.1	72	OHAp-M	Pt-Re-ReO_2	Apt + β-Qtz + Tmag + Melt
ClAp-5[a]	1	1100	0.1	75	ClAp-M	Pt-Re-ReO_2	Apt + β-Qtz + Tmag + Melt

[a] Experiment with a Pt fO_2 sensor (pre-conditioned platinum wire or platinum capsule). Details are provided in Section 3.4.
[b] In this experiment we utilized synthetic $Ca_5(PO_4)_3OH$ in the starting material, however, because we used HF to dissolve the basaltic glass left in the platinum capsule after pre-conditioning, residue enriched in F^- contaminated the experiment, producing apatite close to the FlAp endmember.
[c] Apt = apatite, β-Qtz = beta-quartz, Plag = plagioclase, Px = pyroxene, Ttn = titanite, Tmag = titanomagnetite, Ilm = ilmenite, Fe = Fe metal.

glass SRM 612. Secondary standard analytical recoveries are 0.07 % to 51.58 % of reference values for apatite analysis, and are 0.001 % to 16.22 % of reference values for glass and plagioclase analysis, with an average recovery of 11.26 % and 4.66 %, respectively (Jochum et al., 2011; Jochum et al., 2005; Tables S1 and S2). Analytical results are reported in Tables S3 and S4.

3. Experimental results

3.1. Experimental run products

The mineral products of experiments conducted at 1100 ℃ with C-lined Cr and Mo metal and C-lined Mo capsules included apatite, β-quartz, Fe metal, and quenched glass, while Ca-rich plagioclase and titanite were also observed in experiments ClAp-3 and FlAp8, respectively. For the C-lined Mo experiments conducted at lower run temperatures (1050 ℃), there was no titanite, while ilmenite, pigeonite and clinopyroxene were present, consistent with the mineral assemblage described in Rapp and Draper (2018). For experiments utilizing Pt capsules with Re + ReO_2 layer at 1100 ℃, the experimental products included apatite, titanomagnetite, β-quartz, and quenched glass. No Fe metal was present in those experiments. Among all experiments, no phosphate other than apatite was observed (Fig. 1; Table 2).

Major and trace element concentrations of apatites and melts in each experiment were homogenous or near homogeneous, as evidenced by low standard deviations of averaged core-rim analyses (Tables S3 and S4), and a lack of zoning visible in the backscatter electron images (Fig. 1). No trace element zonation in apatite was observed (see the Yttrium map in Fig. S2). We infer that the relatively long experimental durations and fast diffusion kinetics in apatite and silicate melt (Cherniak, 2000; Cherniak and Ryerson, 1993) produced apatites closely approaching equilibrium with the silicate melt.

3.2. Apatite major element composition

Only one anion component was intentionally added to each initial material (Table 1). The apatite crystallized in each experiment is generally close to each targeted endmember composition (FlAp, OHAp, and ClAp), with the exception of OHAp-7 (see below). In our mineral characterizations, the concentration of hydroxyl (OH^-) was calculated by assuming that the vacancy at X-site is filled by OH^- after considering the amount of Cl^- and F^-. We used the method described by Ketcham (2015) to calculate the apatite mineral formula, which accounts for the OH^- content that can't be directly analyzed by EMP. Different degrees of Cl^- and OH^- contamination were found in our experiments, but the target anion occupancies are always higher than 80 %, except ClAp-1 and ClAp-5 where the Cl^- occupancy are 69 % and 60 % respectively (Table 3). The ClAp experiments are apparently more susceptible to OH^- contamination compared with FlAp experiments, indicating that F generally has a higher apatite-silicate melt partition coefficient compared with Cl (McCubbin et al., 2015a). The OHAp-7 experiment produced apatites containing more than 80 % F^- in X-site because of contamination caused by residue remaining after the HF dissolution following preconditioning of the platinum capsule.

Among all the analyzed apatites, those in ClAp experiments are unique, as they always have higher Na_2O (0.04 – 0.15 wt%), and lower CaO (50.23 – 52.09 wt%) compared with other experiments (where Na_2O varies from 0.01 to 0.08 wt% and CaO from 52.05 to 54.43 wt%). In addition, higher MnO concentration was observed in ClAp (0.31 – 0.41 wt%), consistent with the suggestion of Klement and Haselbeck (1965) that there is a higher solubility of Mn in ClAp. No significant relationship was found between the concentrations of other major elements and the species of anions. Major element concentrations in quenched glass vary because of different mineral assemblages and temperatures, but the quenched glasses in assemblies with C-lined Mo and Cr capsules have lower FeO concentrations (16.72 – 22.18 wt%) than glasses with C-lined Mo capsules (25.98 – 31.22 wt%) conducted at the same temperature. This reflects precipitation of more Fe metal in the lower fO_2 C-lined Mo and Cr experiments. We measured ~ 2 wt% Re in the quenched glass of three experiments conducted in the Re-ReO_2-bearing Pt capsules, despite the extremely low solubility of Re in silicate melt (Ertel et al., 2001). We believe the relatively high Re concentration originates from (1) accidental mixing of Re and/or ReO_2 powders into the experimental powders, as they may adhere to the wall of the capsule during the loading procedure (suggested by the presence of some Pt-Fe-Re alloy on the capsule wall; Fig. 1F), which may accumulate Re micronuggets in the quenched glass, or (2) Re-ReO_2 loss during ultrasonic cleaning and polishing, followed by smearing on the surface of samples, as our experimental dwell temperature is lower than the melting point of the mixture of Re and ReO_2 (Fig. 1C).

Table 3
Unit formulas (cpfu) of apatite and the apatite-silicate melt trace element partition coefficients with 1 sigma uncertainties reported for each experiment.

Sample	FlAp-9	OHAp-1	ClAp-1	FlAp-1	OHAp-6	ClAp-2	FlAp-8	OHAp-5	ClAp-3	FlAp-7	OHAp-7	ClAp-5
cpfu												
Si	0.11	0.13	0.16	0.14	0.11	0.32	0.09	0.32	0.24	0.07	0.09	0.10
Ti	0.01	0.01	0.00	0.01	0.01	0.01	0.01	0.02	0.01	0.00	0.00	0.00
Al	0.00	0.01	0.01	0.00	0.01	0.01	0.01	0.01	0.01	0.01	0.02	0.01
Fe	0.22	0.29	0.36	0.25	0.29	0.30	0.15	0.22	0.25	0.23	0.22	0.20
Mn	0.04	0.04	0.06	0.03	0.03	0.05	0.04	0.04	0.06	0.05	0.05	0.06
Mg	0.03	0.01	0.01	0.04	0.03	0.03	0.03	0.03	0.03	0.06	0.07	0.05
Ca	9.77	9.77	9.55	9.87	9.80	9.45	9.78	9.72	9.68	9.64	9.67	9.73
Na	0.01	0.02	0.05	0.01	0.01	0.04	0.00	0.03	0.04	0.01	0.01	0.01
K	0.00	0.00	0.00	0.00	0.00	0.00	0.00	0.00	0.00	0.00	0.00	0.00
P	5.88	5.83	5.86	5.80	5.84	5.80	5.91	5.72	5.79	5.94	5.91	5.89
F	1.45	0.00	0.00	2.12	0.00	0.00	1.82	0.00	0.00	1.62	1.63	0.00
Cl	0.01	0.01	1.38	0.00	0.07	1.76	0.01	0.08	1.75	0.01	0.01	1.20
OH	0.54	1.99	0.62	0.00	1.93	0.24	0.18	1.92	0.25	0.38	0.36	0.80
D												
Zn	0.11	0.28	0.05	0.25	0.10	0.10	0.24	0.11	0.14	0.27	0.06	0.11
Sr	2.59	1.83	3.01	1.88	1.32	2.00	1.63	1.13	2.08	1.84	1.55	1.50
La	2.44	1.99	0.89	2.22	1.83	0.62	2.06	1.31	0.68	1.35	1.11	0.89
Ce	2.99	2.80	1.13	3.05	2.56	0.88	2.85	1.87	0.98	1.88	1.60	1.20
Pr	3.32	3.36	1.30	3.63	3.11	0.95	3.44	2.25	1.07	2.33	2.02	1.45
Nd	3.38	3.45	1.30	3.46	3.51	0.96	3.86	2.31	1.14	2.59	2.03	1.38
Sm	3.59	3.78	1.36	3.96	3.56	1.12	4.09	2.68	1.19	2.90	2.60	1.51
Eu	2.34	2.29	1.93	2.24	2.08	1.41	2.06	1.42	1.73	2.56	2.28	1.50
Gd	3.78	3.80	1.42	4.06	3.77	1.07	4.93	2.45	1.29	3.23	2.65	1.41
Tb	3.53	3.68	1.21	3.29	3.47	0.83	4.10	2.00	0.92	2.66	2.28	1.14
Dy	3.25	3.09	1.15	3.53	2.90	0.81	3.54	1.88	0.94	2.51	2.15	1.04
Y	3.61	2.81	1.09	3.43	3.02	0.70	3.59	1.89	0.85	2.69	2.38	1.02
Ho	3.46	2.93	1.08	2.89	2.84	0.67	3.47	1.77	0.80	2.49	2.10	1.02
Er	3.14	3.08	1.01	3.20	2.87	0.67	2.80	1.83	0.79	2.50	2.11	0.95
Tm	3.04	2.36	0.95	2.52	2.07	0.57	2.97	1.46	0.62	2.07	1.69	0.80
Yb	2.58	2.15	0.82	2.19	1.89	0.45	2.16	1.31	0.48	1.78	1.49	0.60
Lu	2.77	1.89	0.67	2.45	1.63	0.41	2.09	1.15	0.59	1.72	1.35	0.59
Th	2.50	2.68	0.50	0.91	1.00	0.26	0.85	1.82	0.32	0.65	0.49	0.30
U	2.60	5.85	0.79	0.99	2.35	0.50	1.33	4.23	0.36	0.64	0.53	0.30
σ												
Zn	0.01	–	0.02	0.19	0.02	0.06	0.02	0.01	0.04	0.01	–	0.08
Sr	0.69	–	0.48	0.49	0.07	0.11	0.29	0.20	0.17	0.33	–	0.05
La	0.85	–	0.09	0.10	0.23	0.06	0.22	0.12	0.02	0.28	–	0.03
Ce	1.10	–	0.06	0.15	0.31	0.03	0.38	0.24	0.15	0.43	–	0.05
Pr	0.70	–	0.12	0.17	0.43	0.08	0.19	0.15	0.05	0.54	–	0.14
Nd	1.22	–	0.13	0.26	0.54	0.12	0.22	0.30	0.07	0.55	–	0.10
Sm	0.51	–	0.20	0.52	0.31	0.05	0.66	0.32	0.22	0.65	–	0.10
Eu	0.72	–	0.35	0.42	0.22	0.22	0.45	0.19	0.14	0.74	–	0.15
Gd	1.73	–	0.20	0.49	0.29	0.19	0.56	0.12	0.12	0.71	–	0.07
Tb	1.52	–	0.21	0.38	0.49	0.09	0.33	0.33	0.03	0.63	–	0.10
Dy	1.07	–	0.25	0.29	0.34	0.04	0.23	0.13	0.03	0.55	–	0.03
Y	0.97	–	0.29	0.22	0.34	0.03	0.16	0.15	0.08	0.50	–	0.04
Ho	1.43	–	0.24	0.23	0.34	0.04	0.21	0.21	0.16	0.53	–	0.07
Er	1.11	–	0.26	0.34	0.41	0.08	0.25	0.11	0.02	0.51	–	0.04
Tm	1.08	–	0.44	0.24	0.19	0.08	1.07	0.26	0.03	0.34	–	0.06
Yb	1.07	–	0.36	0.15	0.29	0.04	0.28	0.20	0.18	0.28	–	0.02
Lu	0.68	–	0.39	0.30	0.20	0.09	0.21	0.31	0.10	0.43	–	0.06
Th	1.25	–	0.17	0.52	0.15	0.01	0.35	0.16	0.15	0.22	–	0.02
U	1.35	–	0.07	0.79	0.52	0.15	0.58	0.75	0.09	0.30	–	0.02

3.3. Apatite trace element composition

Apatites in ClAp experiments have lower REE concentrations than apatites in FlAp and OHAp experiments (Fig. S4; Table S3), consistent with the experimental observations described in Fleet et al., (2000a), which found that compared with FlAp and OHAp, ClAp shows about two orders of magnitude lower REE uptake. Different degrees of negative Eu anomalies are observed, and the Eu anomalies are higher among apatites in ClAp experiments (0.38 – 0.58) than those in FlAp and OHAp experiments (0.22 – 0.32). Energy dispersive spectrometric elemental mapping was conducted for one Mo capsule experiment (OHAP-6; Fig. S2A) and one Pt-Re-ReO_2 capsule experiment (OHAP-7; Fig. S2B), using Y as the proxy for REEs. We find no apatite exhibiting obvious elemental zonation.

3.4. Oxygen fugacity of experiments

In our experimental design, we attempted to control fO_2 using three different metal buffers, as accurate knowledge of experimental fO_2s is essential to determine the relationship between fO_2 and Eu anomalies in apatites. Previous work suggests experiments with graphite-lined Mo capsules control the oxygen fugacity close to IW-1 ($C + O_2 = CO_2$; $Mo + O_2 = MoO_2$; e.g., Dygert et al., 2020), while experiments with a Re + ReO_2 layer may produce an $fO_2 \sim 2$ log units above quartz-fayalite-magnetite (QFM) oxygen buffer ($Re + O_2 = ReO_2$; Fabbrizio et al., 2021; Pownceby and O'Neill, 1994). If effective, a Cr metal should

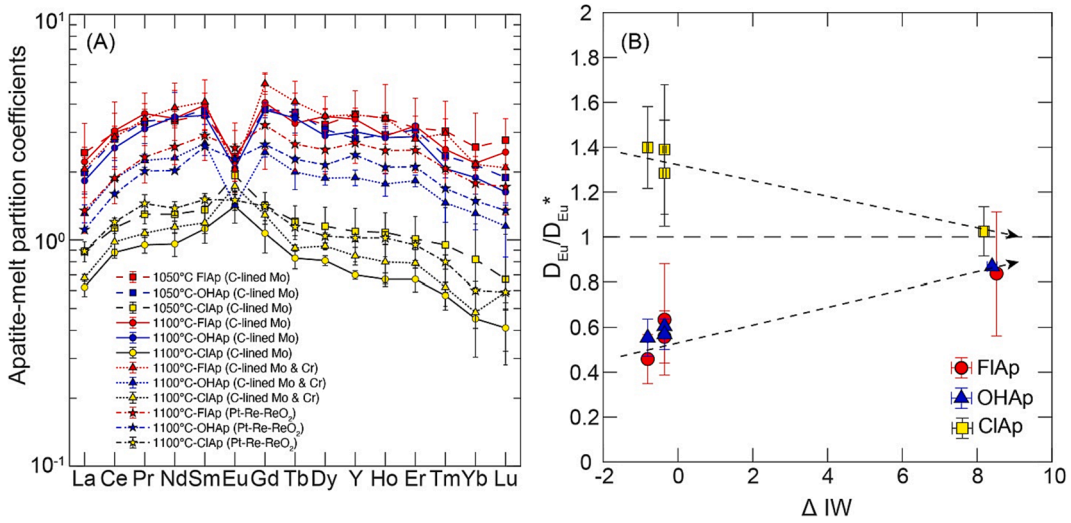

Fig. 2. (A) apatite-silicate melt partition coefficients, and (B) anomalies of partition coefficient of Eu (D_{Eu}/D_{Eu}^*) calculated based on LA-ICP-MS analysis. Red symbols are FlAp experiments, while blue and yellow symbols are OHAp and ClAp, respectively. In Fig. 2A, solid lines show experiments conducted at higher T and C-lined Mo capsules, dotted lines represent the experiments under higher T and C-lined Mo and Cr capsules, and dash-dotted lines are experiments with Pt-Re-ReO_2 capsules. Lowest T experiments are plotted using dashed lines and low fO_2 experiments are plotted using dotted lines. In Fig. 2B, the ClAp showed an opposite trend to OHAp and FlAp, as the partition coefficient of Eu^{2+}in ClAp is higher than that of Eu^{3+}, while in FlAp and OHAp the partition coefficient of Eu^{3+} is higher. All uncertainties are calculated by error propagation.

produce an fO_2 close to IW-5 ($4Cr + 3O_2 = 2Cr_2O_3$; Holzheid and O'Neill, 1995). Rather than assuming our experimental fO_2s are consistent with the metal buffers, we took additional measures to characterize fO_2s for several reasons: (1) the temperature and pressure range recommended for empirical formulas in Pownceby and O'Neill (1994) and Holzheid and O'Neill (1995) differ from the experimental conditions in this study; (2) in Holzheid and O'Neill (1995) the buffer is Cr-Cr_2O_3, while in our experimental products, the Cr metal forms multiple chromium carbide layers, corresponding to different chromium carbide structures (Fig. S3D to S3F). The chromium concentration gradually increases from the rim to the core, but no chromium oxide is observed. (3) In the Pt-capsule samples packed with a layer of Re-ReO_2, the presence of ReO_2 after the experiment was impossible to verify, as most of the Re and/or ReO_2 powder remaining in the experiment fell out of the charges during sectioning and polishing (Fig. 1E).

To address these ambiguities, we used the EMP to analyze the Pt capsules and Pt wires in the experimental run products (Table 3). We calculated the fO_2 from the concentration of Fe in the Fe-Pt alloy according to Eq. (1), based on the method described in Médard et al. (2008):

$$log_{10}fO_2 = \frac{2}{ln(10)}\left[ln\left(\frac{X_{FeO}^{melt}}{X_{Fe}^{alloy}}\right) - ln\left(\gamma_{Fe}^{alloy}\right) + ln\left(\gamma_{FeO}^{melt}\right) - lnK\right], \quad (1)$$

where X_{FeO}^{melt} is the mole fraction of FeO in the melt, and X_{Fe}^{alloy} is the mole fraction of Fe in the alloy. Because Fe is zoned in both platinum wires and capsules (Fig. S3C), we analyzed the compositions of the platinum rim in direct contact with the experiments. We set the FeO activity coefficient γ_{FeO}^{melt} to 1 as suggested by Médard et al. (2008), and we calculate

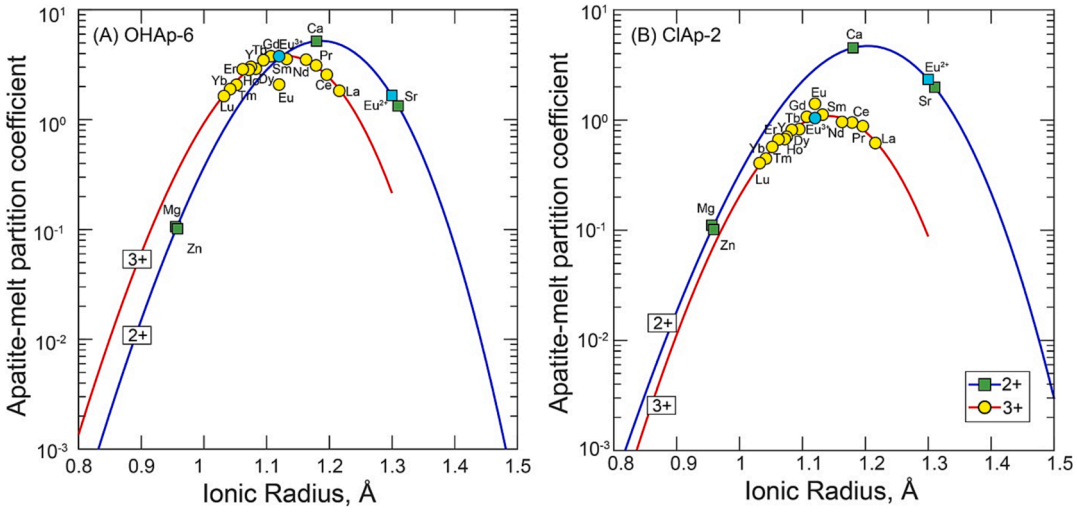

Fig. 3. Onuma diagram showing measured apatite-silicate melt partition coefficients as a function of ionic radius for divalent and trivalent elements derived from experiments (A) OHAp-6 and (B) ClAp-2. The red and blue curves are the best fits to the measured partition coefficients using lattice strain model, and the lattice strain parameters for all experiments in this study can be found in Table 5. The partition coefficients of Eu^{2+} and Eu^{3+} predicted by lattice strain model are also plotted, and the values of measured Eu partition coefficient are always between Eu^{2+} and Eu^{3+}.

the activity coefficient of γ_{FeO}^{melt} and the equilibrium constant K by the empirical formulas in Kessel et al. (2001) and Médard et al. (2008) respectively.

When we analyzed the capsule alloy by EMP, we observed a layer of Pt-Fe-Re alloy at the bottom of the capsule, which forms owing to direct contact of Re metal with the pre-conditioned Pt capsule. Because of the powder loading sequence of the experiments with a Re + ReO_2 layer, there are also small amounts of Re residue in certain areas on the capsule wall, which form an alloy during the experiment (Fig. 1F). Therefore, the measured points selected for constraining the experimental fO_2 are located in the area directly in contact with the starting material without any intervening Re alloy (e.g., Fig. 1C and 1F). The calculated fO_2 data are reported in Table 4. The fO_2 in the experiment with the C-lined Mo capsule (FlAp-9) is IW-0.36, close to the fO_2 suggested by previous studies (e.g., Dygert et al., 2014). However, for Cr metal experiments, the fO_2 that we calculated (~IW-0.81) is much more oxidized than the Cr-CrO_2 buffer (Holzheid and O'Neill, 1995). Apparently, the Cr metal was ineffective for controlling the experimental fO_2 and the fO_2 in FlAP-8 is controlled by the pre-conditioning process. Shown in Fig. 1D, we found a layer of chromium carbide, instead of chromium oxide, formed at the rim of the Cr metal (Fig. 1D and S3E), perhaps providing a barrier that prevented oxidation of the Cr metal and further reduction of the experiment.

For experiments conducted in Pt capsules with a Re + ReO_2 layer, according to the composition of the Fe-Pt alloy, the experiments exhibit the fO_2s varying from FMQ + 4 to FMQ + 4.35, which are about 2 log units higher than anticipated according to the Re-ReO_2 buffer (e.g., Ertel et al., 2001; Fabbrizio et al., 2021). We analyzed the Fe concentration in the ClAp-5 Pt capsule and found from the inner wall (in direct contact with the initial compositions) to the outer wall (in direct contact with MgO), the concentration of Fe first decreases and then increases, and the composition varies continuously (Fig. S3C). The outer wall reflects the alloyed condition after the capsule pre-conditioning process, conducted in a relatively reducing atmosphere, while the inner wall exhibits a lower Fe concentration, suggesting the starting material powders were conditioned in a more oxidizing atmosphere. This led to oxidation of Fe metal initially alloyed with the Pt capsule. We infer that the higher than anticipated fO_2 calculated from the Fe-Pt alloy reflects the experimental fO_2, and attribute the target and experimental fO_2 discrepancy to inconsistencies in the pre-conditioned fO_2s of starting material powders and capsules. In the main text, we report fO_2s determined from the Fe-Pt alloy, in Table S5, we report fO_2 according to the Re-ReO_2 buffer. We note that because the experiments are oxidized in either case, the impact of this fO_2 uncertainty on our new predictive models (presented in Section 4.3.4) is negligible (Table S5). In conclusion, according to the Fe concentrations in Pt, our efforts produced ~ 9 orders of magnitude variation in fO_2 among the experiments owing to the different assembly types and conditioning procedures (Table 4).

3.5. Apatite-silicate melt partition coefficients

Using the trace element concentrations acquired by LA-ICP-MS analysis, we calculate partition coefficients for REEs between apatite and silicate melts (Table 3; Fig. 2). Consistent with the elemental concentrations, the REE partition coefficients of apatites in OHAp and FlAp experiments are similar at a given temperature, and those for ClAp are a factor of two to four lower depending on the experiment (yellow symbols in Fig. 2A), in agreement with the trend reported in Fleet et al., (2000a). Apatites in ClAp experiments exhibit positive Eu partition coefficient anomalies (D_{Eu}/D_{Eu}^* = 1.03 – 1.40, where D_{Eu}/D_{Eu}^* is defined here as $D_{Eu}/\sqrt{D_{Sm} \times D_{Gd}}$), compared with apatites in FlAp and OHAp experiments (where D_{Eu}/D_{Eu}^* varies from 0.46 to 0.87; Fig. 2B). It is also worth noting that the partition coefficient of Eu is much less affected by X-site occupancy than other REEs, indicating that the influence of X-site occupancy on trivalent elements is greater than that of divalent elements (Fig. 2A).

Temperature also apparently affects the partition coefficients, as the experiments show that the lower the temperature, the higher the partition coefficient (Fig. 2A), as suggested by Watson and Green (1981). In lower fO_2 experiments (C-lined Mo and Cr capsule), the D_{Eu}/D_{Eu}^* becomes more obvious (Fig. 2B). No systematic effect of fO_2 on partition coefficients of other REEs, including Ce, was observed. The divalent elements show a regular pattern, as the element with the highest partition coefficient is always Ca, and the partition coefficients have no obvious relationship with the anion occupancy (Table 3). Discussion of trivalent and divalent substitution mechanisms can be found in Sections 4.3.1 and 4.3.2.

4. Discussion

4.1. Insights into cation site occupancies from application of the lattice strain model

Systematic variations of isovalent cation partition coefficients between minerals and melt have been observed in Onuma diagrams as a function of ionic radius (Onuma et al., 1968). These parabolic trends can be effectively described using the lattice strain model (e.g., Brice, 1975; Blundy and Wood, 1994):

$$D_i^{min-melt} = D_o exp\left[\frac{-4\pi E N_A}{RT}\left(\frac{r_o}{2}(r_o - r_i)^2 - \frac{1}{3}(r_o - r_i)^3\right)\right], \quad (2)$$

where $D_i^{min-melt}$ is the mineral-melt partition coefficient of element i; D_o is the strain-free partition coefficient; E is the effective Young's modulus; r_o is the ideal ionic radius in Å; r_i is the ionic radius of substituting element, and for apatite predictive models here we choose radius in IX-fold coordination, consistent with the Ca1 site; R is the gas constant; N_A is Avogadro's number and T is the temperature in Kelvin.

Table 4
Calculated oxygen fugacities for experiments based on Pt-Fe alloy compositions.

Run	Conditions									fO_2		
	T (°C)	Attempted buffer	n[a]	Fe (wt.%)	Pt (wt.%)	Total (wt.%)	X_{Fe}^{alloy}	X_{Pt}^{alloy}	X_{FeO}^{Melt}	logfO_2	ΔIW	ΔFMQ
FlAp-8	1100	Cr	6	69.15	26.9	96.05	0.90	0.10	0.15	−13.73	IW-0.81	FMQ-4.99
σ[b]				1.16	1.17		0.004	0.004	0.003	0.02	0.02	0.02
FlAp-9	1050	Mo	6	63.49	34.4	97.89	0.87	0.13	0.21	−14.02	IW-0.36	FMQ-4.62
σ				2.08	2.3		0.011	0.011	0.001	0.04	0.04	0.04
OHAp-7	1100	Re + ReO_2	6	4.13	93.05	97.18	0.13	0.87	0.22	−4.51	IW + 8.40	FMQ + 4.23
σ				0.62	1.77		0.011	0.011	0.003	0.13	0.13	0.13
FlAp-7	1100	Re + ReO_2	5	3.57	93.07	96.64	0.12	0.88	0.18	−4.40	IW + 8.52	FMQ + 4.35
σ				0.07	1.08		0.012	0.012	0.002	0.02	0.02	0.02
ClAp-5	1100	Re + ReO_2	6	4.07	91.38	95.45	0.13	0.87	0.17	−4.74	IW + 8.18	FMQ + 4.00
σ				0.53	1.57		0.008	0.008	0.001	0.10	0.10	0.10

[a] Number of EMP analyses.
[b] The σ takes into account analytical uncertainties and is calculated through the propagation of uncertainty formula. Uncertainties in the model inputs used apply Eq. (1) are not reported, such that we cannot comprehensively estimate the uncertainties of calculated fO_2s.

Table 5
Lattice strain parameters calculated from experiments in this study using ninefold ionic radii.

Run	E^{2+} (GPa)	ro^{2+} (Å)	Do^{2+}	E^{3+} (GPa)	ro^{3+} (Å)	Do^{3+}
FlAp-9	177	1.198	6.86	111	1.123	3.71
σ	15	0.004	0.14	13	0.003	0.07
OHAp-1	169	1.182	6.10	203	1.130	3.87
σ	3	0.001	0.03	17	0.002	0.09
ClAp-1	177	1.216	5.99	167	1.137	1.41
σ	18	0.003	0.17	12	0.002	0.02
FlAp-1	173	1.193	5.08	175	1.131	3.95
σ	13	0.004	0.09	24	0.003	0.13
OHAp-6	215	1.187	5.16	242	1.130	3.81
σ	2	0.001	0.01	18	0.002	0.09
ClAp-2	181	1.204	4.75	242	1.141	1.09
σ	3	0.001	0.02	21	0.002	0.03
FlAp-8	182	1.190	4.87	253	1.126	4.48
σ	17	0.006	0.11	25	0.002	0.14
OHAp-5	187	1.189	3.55	224	1.135	2.54
σ	1	0.000	0.00	20	0.002	0.07
ClAp-3	177	1.204	4.85	230	1.140	1.23
σ	6	0.002	0.04	27	0.003	0.04
FlAp-7	170	1.191	5.03	214	1.120	3.01
σ	11	0.004	0.09	19	0.002	0.07
OHAp-7	201	1.195	4.79	229	1.121	2.58
σ	16	0.004	0.08	21	0.002	0.07
ClAp-5	189	1.193	4.47	230	1.144	1.56
σ	5	0.001	0.03	19	0.002	0.04

We use the nonlinear regression method to calculate the lattice strain parameters (D_o, E, and r_o) of divalent and trivalent elements for each experiment (Table 5). For each parabola, we use at least three partition coefficients of isovalent elements to define the parabola and ensure the partition coefficients do not vary monotonically with the ionic radius, in order to better constrain the ideal radius (r_o). All the divalent elements and trivalent elements, except Eu, display parabolic patterns in ninefold coordination (e.g., Fig. 3), supporting the quality of our data. In the apatite structure, there are two Ca sites where REEs can potentially reside, one is sevenfold coordination (Ca2), and the other is ninefold (Ca1). The site preference for REEs is controversial. A Ca2 preference has been proposed by Borisov and Klevtsova (1963), while Urusov and Khudolozhkin (1974) argue for Ca1 occupancy. Cockbain and Smith (1967), however, advocate for no preference for REE occupancy in either Ca site in apatite. When examining our data, we applied ninefold coordination. Shannon (1976) did not report sevenfold ionic radii for some REEs, such that using ninefold coordination avoids errors caused by extrapolating the sevenfold ionic radii and the propagation of related errors in the models. For divalent cations, because Shannon (1976) did not report the radii of IX-coordinated Mg and Zn, we calculated their ninefold radii based on an extrapolation between eightfold and ninefold coordinated ionic radii for other divalent cations (Fig. S5).

We find that the ideal ionic radii of trivalent elements (r_o^{3+}) are smaller than divalent elements (r_o^{2+}), which suggests the trivalent elements tend to enter the smaller Ca2 site and divalent elements prefer to substitute into the larger Ca1 site (Fig. 3; Table 5). Nonetheless, for the aforementioned reasons, we model all divalent and trivalent elements in all apatites using ninefold ionic radii. We note that ClAp experiments exhibit larger ideal radii (1.137 to 1.144 Å; Fig. 4A) for the trivalent elements (without Eu) compared to those in FlAp and OHAp (1.120 to 1.135 Å; Fig. 4A; Table 5), perhaps suggesting that REEs in ClAp prefer larger Ca1 sites, while in FlAp and OHAp, they enter the smaller Ca2 site. This observation is consistent with previous analysis of experiments conducted by Fleet et al., (2000a), Fleet et al., (2000b), and Fleet and Pan (1997), which used single crystal X-ray measurement to analyze high-temperature synthetic apatite. They calculated the atomic position and isotropic displacement parameters of apatite, which suggested the REEs prefer the Ca2 site in FlAp and OHAp, and that the ratio of Ca2 occupancy will decrease with the decrease of ionic radius through the lanthanide series (Pan and Fleet, 2002). Because the radius of Cl^- is

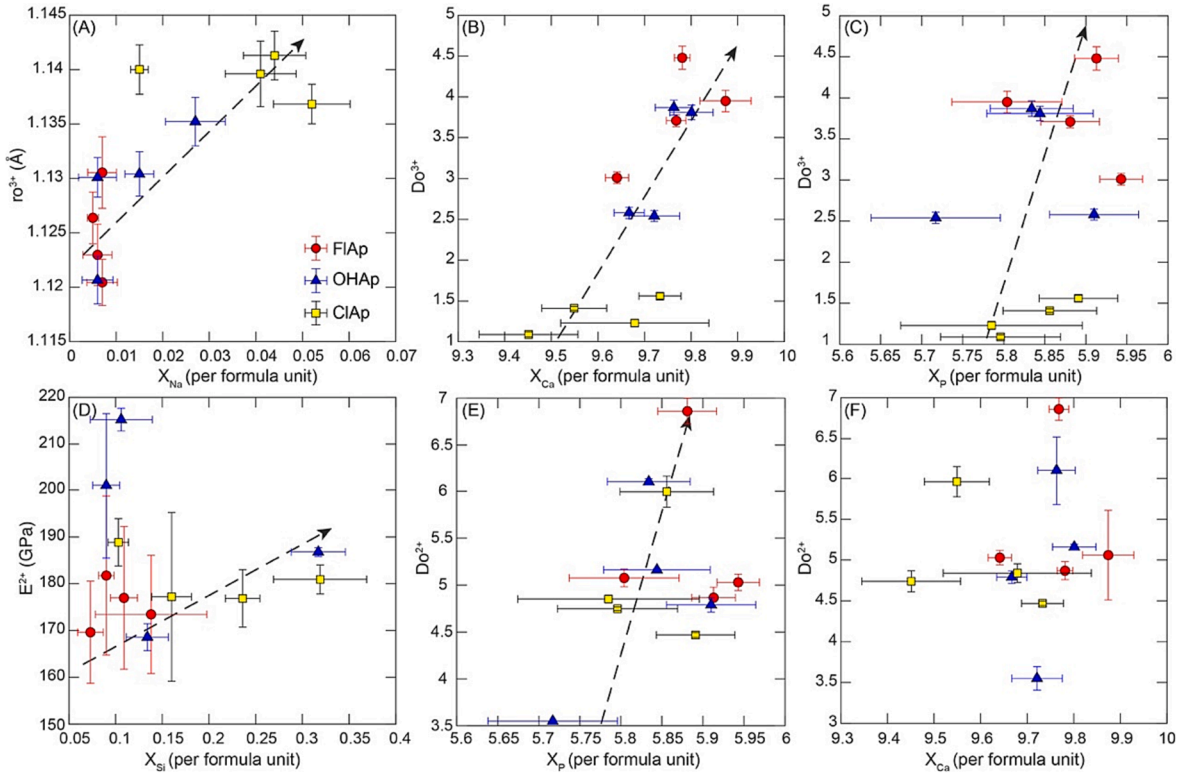

Fig. 4. Lattice strain terms plotted against selected apatite cation site occupancies for trivalent elements (A) - (C) and divalent elements (D) - (F). All the data can be found in Table 5. The trends between lattice strain parameters of trivalent trace elements and major elements (Ca, Si, and P) agree with substitution mechanisms (13)–(15), while the lattice strain parameters of divalent elements are poorly correlated with X_{Ca} (F), but relatively well correlated with Si and P cations (D-E).

larger than that of F^- and OH^- (Shannon, 1976), in ClAp the REEs prefer to occupy the Ca1 site (Fleet et al., 2000a), which accommodates proportionally more light-REEs than the Ca2 site, as suggested by higher D_{La} / D_{Yb} in ClAp experiments (1.09 to 1.48) than FlAp and OHAp (0.75 to 1.01). Because the radii of F^- and OH^- are similar, the REE partitioning behavior of OHAp and FlAp are very similar. The much lower REE partition coefficients in ClAp experiments suggest the expansion of the Ca2 sites because of the occupancy of larger Cl^-, thereby making Ca2 less suitable for REE substitution (Fig. 4C; Fleet et al., 2000a). A similar inference can be made from the lattice site parameters of divalent cations (Table 5), but the trends are not as obvious as from the trivalent parameters.

4.2. Calibrating dataset for predictive trace element partitioning models

In order to develop predictive trace element partitioning models for apatite and silicate melts, we compiled data from previous published experimental studies (Prowatke and Klemme, 2006; Stepanov et al., 2023; Tailby et al., 2023; Watson and Green, 1981), and data from an apatite-melt inclusion partitioning study (Li et al., 2023), in addition to our new apatite-melt experiments. The experimental data we used to develop our predictive models include 29 experiments and 1 apatite-melt inclusion pair for a total of 292 trivalent and 92 divalent partition coefficients. Tailby et al. (2023) recently reported a series of apatite-melt partitioning data at 1 bar. They used five different capsule types in order to evaluate the effect of fO_2 on Eu partitioning from IW to HM buffer. However, they did not mention whether they preconditioned their starting materials. Some apatites exhibit compositional anomalies in major element analysis (e.g., ApREE-03a (NNO), ApREE-03b (MMO), ApREE-04 (HM) and ApREE-15A-02). For these reasons we only include two of their experiments applying graphite capsules in our compilation (ApREE-09 and ApREE-12; Tailby et al., 2023). The apatite-silicate melt partitioning experiments from Li and Hermann, 2017 were not considered here for several reasons: (1) as Li and Hermann (2017) pointed out in the description of their method, the grain sizes of their apatites are too small (1–5 μm) for single phase analyses by LA-ICP-MS such that the apatite measurements are actually the mixture of apatite and melt. Corrections were applied to remove the glass contribution from the apatite analyses, but the accuracy of the data cannot be guaranteed; (2) the run temperature of their experiments is very low (800 ℃), and their experimental durations were not reported. In this circumstance, it is impossible to evaluate whether apatite is in equilibrium with melt, as zonation may exist in their apatites which were analyzed in bulk. (3) In their experimental results, significant anomalies relative to Onuma fits exist (e.g., C3927, C4049, C4059), suggesting chemical disequilibrium and/or analytical issues.

The compiled data used to parameterize our partitioning models are summarized in the Supplementary Materials. We compiled as many trivalent (REE + Y) and divalent element (Mg, Zn, Ca, and Sr) partition coefficients as possible, however, we did not consider Ba, because of its low concentration in apatite and correspondingly large analytical uncertainty. All the data we compiled include at least three partition coefficients for elements in the same valence state (Fig. 3), which is required to establish lattice strain parabolas for individual experiments given the three unknowns in the lattice strain model (Eq. (2); Wood and Blundy, 1997).

4.3. Predictive trace element partitioning models

4.3.1. Trivalent element model

In order to constrain the parameters that can strongly affect the D_o, E, and r_o, we considered temperature (Watson and Green, 1981) and pressure (Supplementary Fig. S6), as well as compositional terms, as candidates. We tested the contribution of these candidate parameters by simultaneous inversion until we obtained a parameter combination that returned the best overall fit (e.g., Yao et al., 2012). We used Pearson's Chi-square (defined below) to evaluate the fitting effect as described in Sun and Liang (2012):

$$\chi_p^2 = \sum_{i=1}^{N} \frac{\left(D_i^p - D_i^m\right)^2}{D_i^p}, \tag{3}$$

where D_i^p and D_i^m are the modeled, and measured mineral-melt partition coefficients of element i respectively. The predictive model with the best fit returns the smallest χ_p^2 value.

Applying the lattice strain model to 292 experimental trivalent element partitioning data (Prowatke and Klemme, 2006; Stepanov et al., 2023; Tailby et al., 2023; Watson and Green, 1981; this study), and one apatite-melt inclusion pair from Li et al. (2023), we obtain the following expressions that maximize the quality of the fit:

$$ln\mathrm{D}_o^{3+} = -194.75(\pm 14.73) + \frac{6.66(\pm 1.46)}{RT} \times 10^4 + 8.10(\pm 0.77)X_{Ca} + 14.16(\pm 1.47)X_{Si} + 18.62(\pm 1.66)X_P, \tag{4}$$

$$E^{3+}(\mathrm{GPa}) = -2.17(\pm 1.00) \times 10^3 + 417(\pm 170)X_P, \tag{5}$$

$$r_o^{3+}(\text{Å}) = 1.134(\pm 0.002) + 0.137(\pm 0.030)X_{Na}, \tag{6}$$

where X_{si}, X_{Ca}, X_{Na} and X_P are the Si, Ca and P contents in apatite per formula unit (Table 2). Values in parentheses are 1 σ uncertainties in the model coefficients (see the Supplementary Materials for details). No significant relationship between experimental pressure and lattice strain parameters was observed (Fig. S6). Adding more fitting parameters may further improve the quality of the fit (e.g., melt composition terms), but the model we developed fits the measured partitioning data well, and has the advantage of using major element composition of apatite only to successfully reproduce the partition coefficients from this study and previous work (Fig. 5A).

The compositional terms in our predictive model are consistent with substitution mechanisms proposed in previous studies. The Si, Ca, and P contents in apatite play an important role in the partitioning behavior of REEs in FlAp and OHAp, which can be explained by following two substitution mechanisms (Watson and Green, 1981; Chen et al., 2002):

$$REE^{3+} + Si^{4+} = Ca^{2+} + P^{5+}, \tag{7}$$

$$2REE^{3+} + [v] = 3Ca^{2+}, \tag{8}$$

where [v] represents a cation vacancy. The above mechanisms are suggested by correlations between lattice strain parameters in FlAp, OHAp and X_{Ca}, X_P in apatite (Fig. 4B and 4C), where apatite with more Ca and higher P concentrations also have higher REE partition coefficients. According to the suggestion by Fleet et al., (2000a), a parallel substation mechanism that controls the REE partitioning in ClAp is:

$$REE^{3+} + Na^{+} = 2Ca^{2+}, \tag{9}$$

which can explain the higher Na_2O concentration in ClAp as shown in Fig. 4A. The relatively low X_{Ca} in ClAp (Fig. 4B) can be also explained by the mechanism above, as the intake of one REE^{3+} corresponds to expulsion of two Ca cations, higher than the REE^{3+}: Ca^{2+} ratio in Eqs. (7) and (8).

4.3.2. Divalent element partitioning model

Applying the lattice strain model to 92 partitioning data from 26 experiments (Prowatke and Klemme, 2006; Watson and Green, 1981; this study), and one apatite-melt inclusion pair from Li et al. (2023), we obtain the following expressions that maximize the quality of the fit:

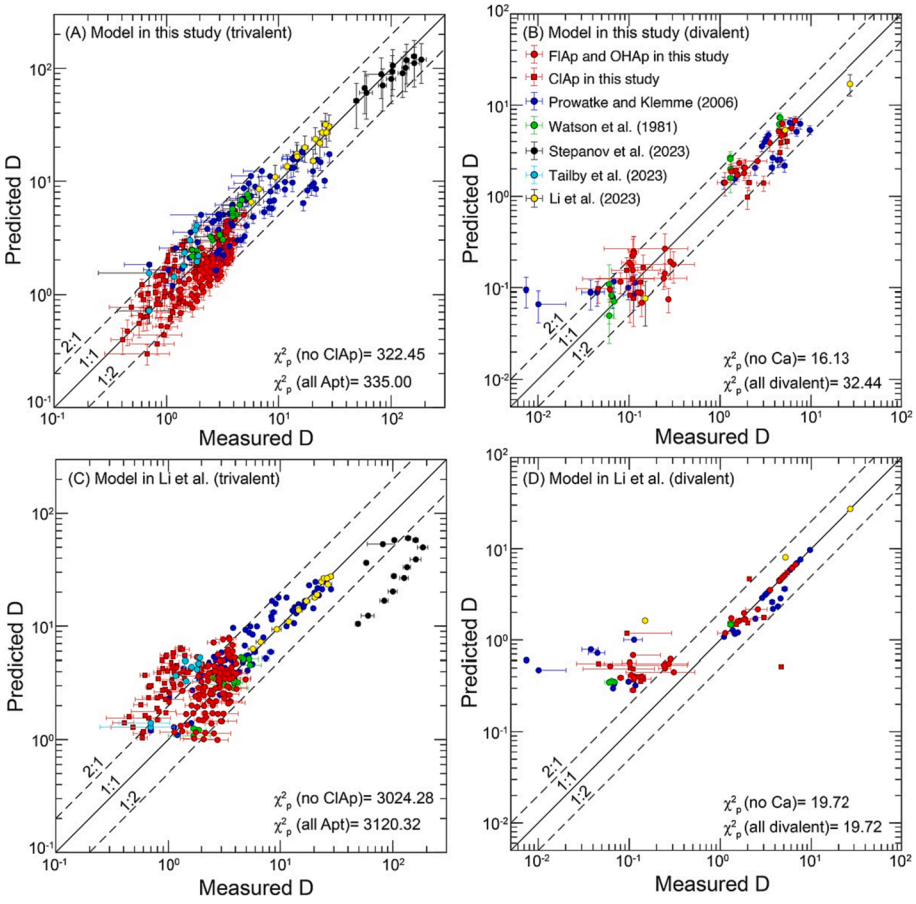

Fig. 5. Comparison between measured partition coefficients and partition coefficients calculated by Eqs. (3), (4–6) and (10–12) for trivalent elements and divalent elements by (A-B) our predictive models and (C-D) predictive models in Li et al. (2023). The error bars represent one sigma error, and the calculation details can be found in the Supplementary Materials. Considering the uncertainties, almost all predicted trivalent and divalent elements fall within the 2:1 and 1:2 dashed lines (A-B). The trivalent predictive model of Li et al. (2023) (C) cannot reproduce apatites in ClAp experiments (red squares) or apatite in low temperature experiments (black circles) and returns χ_p^2 values about an order of magnitude higher than χ_p^2 values of predictive model in (A), with or without considering the ClAp data. The divalent predictive model of Li et al. (2023) (D) shows less bias associated with anionic occupancy, but fails to reproduce Zn and Mg partition coefficients. We note that in (D), the model of Li et al. (2023) returns an apparently lower χ_p^2 than our model, because the model requires input of the partition coefficient of Ca (the perfectly fit elements on the 1:1 line). If we compare the fitness for elements excluding Ca, our model in (B) returns a χ_p^2 value of 16.13, smaller than 19.72 in (D).

$$lnD_o^{2+} = -61.93(\pm 16.96) + \frac{6.58(\pm 1.52)}{RT} \times 10^4 + 2.54(\pm 0.87)X_{Ca} + 3.22(\pm 1.78)X_{Si} + 5.57(\pm 1.75)X_P, \quad (10)$$

$$E^{2+}(\text{GPa}) = -2.47(\pm 1.23) \times 10^3 + 449(\pm 204)X_P + 208(\pm 177)X_{Si}, \quad (11)$$

$$r_o^{2+}(\text{Å}) = 0.818(\pm 0.276) + 0.065(\pm 0.047)X_P, \quad (12)$$

where numbers in parentheses are 1 σ uncertainties. Although we included predictions of the major element Ca in the divalent model (which should deviate from Henrian mixing behavior relevant to trace elements), the lattice strain-based model still effectively predicts the partition coefficients of Ca and other divalent trace elements. Consistent with discussion in Li et al. (2023), we found the influence of pressure on the trace element partitioning is insignificant compared to temperature and composition, and therefore we did not add the pressure term in our models (Fig. S6).

According to previous work, the substitution mechanism for divalent cations is more straightforward than for trivalent ions (e.g., Pan and Fleet, 2002). As the same valence state with Ca^{2+}, divalent cations will substitute in the Ca site directly:

$$M^{2+} = Ca^{2+}. \quad (13)$$

However, direct exchange between the divalent element and Ca cannot explain the partitioning behavior we observed in entirety, otherwise divalent elements in apatite should be correlated with the Ca abundance (Fig. 4F). This complexity was pointed out in the elemental diffusion study of apatite by Cherniak and Ryerson (1993).

The divalent cations that we evaluated prefer to enter larger Ca1 sites according to our predictive model (Fig. 3). In previous studies, strontium has been considered to primarily occupy the Ca2 site (e.g., Hughes et al., 1991), but Sudarsanan and Young (1980) suggested the Ca2 preference will decrease as the concentrations of Sr in apatite increase. Experimental work indicates Mg prefers to enter Ca1 site and can be exchanged with REE (Ito, 1968). Likewise, as the major substituting ion for REE, predictions of partitioning of Ca^{2+} should consider the trivalent substitution mechanisms above, as more Ca in apatite can facilitate Eqs. (7)-(9), and REEs are often a major component in natural apatites.

Anion site occupancy will also affect divalent cation partitioning, as Cl^- is larger than F^- and OH^-, and the Ca2 substitution of divalent cations will be restricted in ClAp by distorting or shrinking the Ca2 site (Fig. S1). It can be seen that the overall structure of apatite and the combined contribution of several mechanisms, rather than merely considering Ca cation in the structure, contribute to the substitution of divalent cations. In this light, we added X_P and X_{Si} to our predictive models to improve the

quality of the fit. Covariation of these terms with lattice strain parameters for divalent elements (Fig. 4D and 4E) suggests they may significantly contribute to divalent element partitioning, in addition to X_{Ca}, or perhaps these elements represent a proxy for structural changes that affect divalent element partitioning.

4.3.3. Comparison with another predictive model

A recent study developed an apatite trace element partitioning model and a Eu-in-apatite oxybarometer (Li et al., 2023). The models of Li et al. (2023) are calibrated using partition coefficients between FlAp and alkaline melts in natural samples, with no ClAp data in their calibrating dataset, thus, predictions made using these models for ClAp and OHAp are extrapolations. All of their models, including the divalent predictive model, trivalent predictive model and Eu-in-apatite oxybarometer, require knowledge of the melt composition in equilibrium with the apatite, limiting application to magmatic processes, and excluding application to subsolidus systems. We used the trace element predictive models of Li et al. (2023) to reproduce our experimental results (Fig. 5C and 5D). Predictions for FlAp and OHAp are mostly accurate within a factor of two, but the predictions exhibit a scattered distribution with a systematic overestimation of REE partition coefficients for all ClAp, and underestimation of apatite-melt partition coefficients for low temperature experiments (800 ℃; Stepanov et al., 2023; Fig. 5C). The divalent model of Li et al. (2023) is calibrated by Ca, Sr, and Ba partitioning data, and overestimates measurements when extrapolated to predict Mg and Zn partition coefficients (Fig. 5D). We calculated Pearson's Chi-square for Li's models by Eq. (3), and the χ_p^2 of each model is reported in Fig. 5C and 5D. Our trivalent predictive model shows about an order of magnitude smaller χ_p^2 values with or without the ClAp data. We note that when we compare χ_p^2 values of divalent models, we must recalculate the χ_p^2 value of our model by removing the Ca in Fig. 5B, because the predictive model in Li et al. (2023) requires the input of the Ca partition coefficient between apatite and silicate melt, such that the fit of Ca is always apparently perfect. After the re-calculation excluding Ca, the χ_p^2 of our divalent model is 16.13, in contrast to 19.72 using the model of Li et al. (2023). Note that we did not normalize χ_p^2 of models in Li et al. (2023) and this study, as for both divalent and trivalent models, the quantities of elements compared are consistent.

We infer our model produces an improved fit to the data for two reasons: (1) the models of Li et al. (2023) were parameterized using fluorapatite data, and they assumed two lattice strain parameters (r_o^{3+} and E^{3+}) are constants, which is acceptable for FlAp and OHAp because of their similar anion radii, but not for ClAp which has larger anion radius (Shannon, 1976). As discussed in Section 4.3.1, different apatite X-site occupancy and cation species can both affect the substitution mechanisms and the Ca site preference, thereby modifying r_o^{3+} and E^{3+}. (2) The predictive model of Li et al. (2023) is based on temperature and the composition of the silicate melt, but the melt composition can't directly reflect the differences in apatite structure, or coupled substitution mechanisms that produce differences in partitioning between FlAp and ClAp-bearing systems.

4.3.4. Eu anomalies and Eu in apatite-plagioclase oxybarometer

Due to the strong dependence of the valence state of the middle REE Eu on oxygen fugacity, Eu fractionation can provide a reliable method to probe the fO_2 of a magmatic system (e.g., McCanta et al., 2009; Wadhwa, 2001). This is supported by our experimental results which demonstrate the higher the fO_2, the closer the partition coefficient of Eu is to the Eu^{3+} partition coefficient and the closer D_{Eu}/D_{Eu}^* is to 1 (Fig. 2B). For FlAp and OHAp, divalent Eu has a lower partition coefficient than trivalent Eu, causing an overall Eu partitioning trend opposite to ClAp experiments, which show $D_{Eu}/D_{Eu}^*>1$, and larger D_{Eu}/D_{Eu}^* magnitudes with decreasing fO_2 (Fig. 2B). Regardless of the anion occupancy, the ratio of Eu^{2+} to Eu^{3+} in apatite is closely related to the fO_2, such that here, we develop an fO_2-dependent Eu partitioning model for apatite and silicate melts.

Eu partitioning between apatite and silicate melts involves both divalent and trivalent Eu. We express the Eu species in the melt by the following reaction (e.g., Drake, 1975):

$$Eu^{3+}O_{1.5} = Eu^{2+}O + \frac{1}{4}O_2. \tag{14}$$

Here we define a constant $K_{Eu}^{apt-melt}$ to represent the heterogeneous equilibrium for the silicate melt in equilibrium with apatite. The partition coefficient of Eu between apatite and silicate melt can be expressed as the function of $K_{Eu}^{apt-melt}$, fO_2, and the partition coefficient of Eu^{2+} and Eu^{3+} in apatite (e.g., Dygert et al., 2020; Mallmann et al., 2021):

$$D_{Eu}^{apt} = \frac{K_{Eu}^{apt-melt} \times D_{Eu^{2+}}^{apt} + D_{Eu^{3+}}^{apt} \times (fO_2)^{\frac{1}{4}}}{K_{Eu}^{apt-melt} + (fO_2)^{\frac{1}{4}}}, \tag{15}$$

where $D_{Eu^{2+}}^{apt}$ and $D_{Eu^{3+}}^{apt}$ are partition coefficients of Eu^{2+} and Eu^{3+} between apatite and silicate melts that can be calculated by our predictive models in Sections 4.3.1 and 4.3.2. Through fitting compiled experimental and natural apatite-melt partitioning data (see Section 4.2), we determined the $K_{Eu}^{apt-melt}$ by nonlinear least squares regression:

$$K_{Eu}^{apt-melt} = 6.20 \times 10^{-4} \pm 9.61 \times 10^{-5}. \tag{16}$$

By applying the $K_{Eu}^{apt-melt}$ value, we can calculate the D_{Eu}^{apt} and compare the results with measured partition coefficients in this study, Li et al. (2023) and Tailby et al., (2023) (Fig. 6A). Considering the analytical and model uncertainties, our calculations show a good agreement between the experimental and predicted D_{Eu}^{apt} at the relevant fO_2.

Through rearranging the Eq. (15), we obtain a new equation that enables us to calculate fO_2 by $K_{Eu}^{apt-melt}$, predicted $D_{Eu^{2+}}^{apt}$ and $D_{Eu^{3+}}^{apt}$ (Eqs. (2), 4–6, and 10–12), and D_{Eu}^{apt} acquired directly from analysis:

$$\log fO_2 = -4 \times log\left(\frac{D_{Eu^{3+}}^{apt} - D_{Eu}^{apt}}{K_{Eu}^{apt-melt} \times \left(D_{Eu}^{apt} - D_{Eu^{2+}}^{apt}\right)}\right). \tag{17}$$

We note application of Eq. (17) is meaningless if the predicted $D_{Eu^{2+}}^{apt}$ and $D_{Eu^{3+}}^{apt}$ are higher or lower than measured D_{Eu}^{apt} (e.g., Dygert et al., 2020). Because the difference between $D_{Eu^{2+}}^{apt}$ and $D_{Eu^{3+}}^{apt}$ is usually relatively small compared to analytical uncertainty for D_{Eu}^{apt} analysis in a natural sample (Fig. 3), uncertainties in measurement of the Eu partition coefficient strongly affect the accuracy of the oxybarometer. This was also observed by Tailby et al. (2023), making the oxybarometer ineffective in oxidized systems (note that the blue curve in Fig. 7 flattens at fO_2s more oxidizing than the FMQ buffer).

Taking advantage of our experimental constraints on the partitioning behavior of Eu in apatite, and a published model for Eu partitioning in plagioclase (Dygert et al., 2020), we developed a Eu in apatite-plagioclase oxybarometer (red line, Fig. 7). Underlying assumptions are that both phases are saturated in the system and they are in equilibrium. Thus, the equilibrium constant of Eq. (16), which defines the Eu speciation in coexisting liquid in the system as a function of fO_2, should be the same for both apatite and plagioclase. Given the very limited amount of experimentally constrained coexisting apatite and plagioclase data, and observation that our calculated $K_{Eu}^{apt-melt}$ (Eq. (16) is similar to value of $K_{Eu}^{plag-melt}$ reported in Dygert et al. (2020), we utilized apatite-silicate melt and plagioclase-silicate melt partitioning data from different experiments to fit a single equilibrium constant for the two phases ($K_{Eu}^{apt-plag}$) simultaneously. We compiled the Eu partitioning data from 15 experiments and an inclusion-host pair (Li et al., 2023, Tailby et al., 2023, and this study), and 25 plagioclase data (Aigner-Torres et al., 2007, Bindeman and Davis, 2000, Dygert et al., 2020, Tepley III et al., 2010, McKay et al., 1994, Sun et al., 2017, and this study;

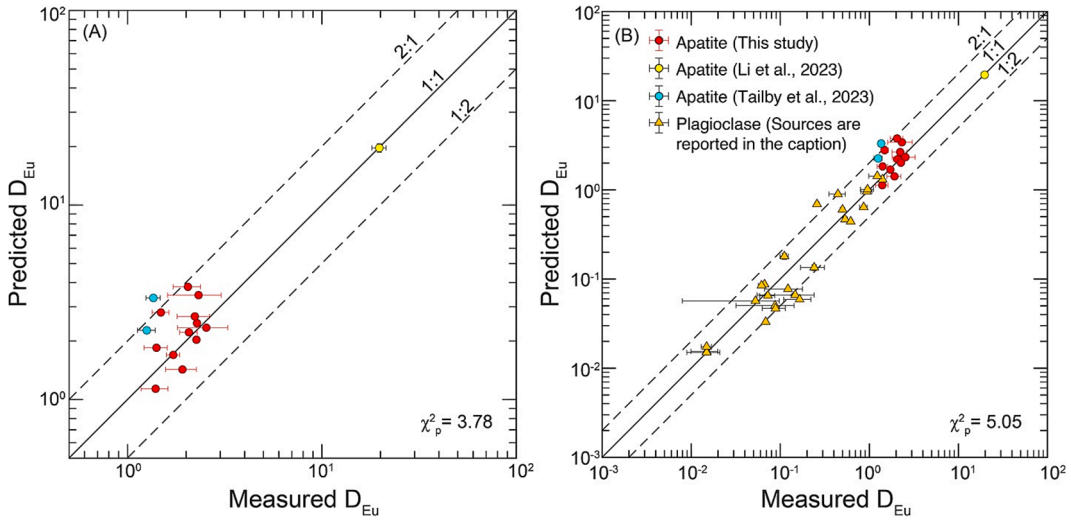

Fig. 6. Comparison between measured and predicted partition coefficients of Eu. (A) D_{Eu} predictions calculated using a model calibrated only using the partition coefficient between apatite and silicate melt (Eqs. 15, 16); predictions shown in (B) are calculated using an equilibrium constant constrained using apatite-melt and plagioclase-melt partitioning data (Eqs. 18, 19). Plagioclase data are the calibrating dataset from Dygert et al. (2020), and include Sun et al. (2017), Aigner-Torres et al. (2007), Bindeman and Davis (2000), Tepley III et al. (2010), and McKay et al. (1994) (Table S6).

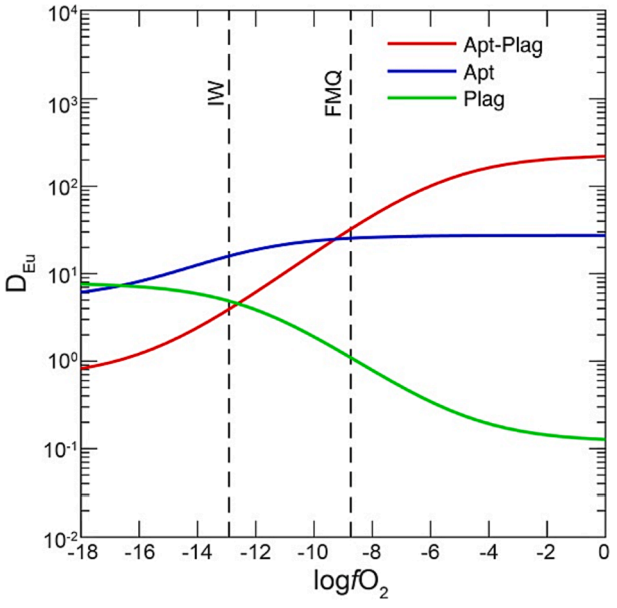

Fig. 7. Predicted partition coefficients of Eu as a function of oxygen fugacity for Eu-in-apatite (Eq. (17), Eu-in-plagioclase and Eu in apatite-plagioclase (Eq. (18) calculated using major element compositions of phases in winonaite HaH 193 (Table S7). The slope of the apatite-plagioclase partitioning behavior is much steeper than that of apatite over a wide range of fO_2s, making a successful model of Eu in apatite-plagioclase partitioning behavior effective as a mineral–mineral oxybarometer.

Table S6), to determine the best fit to the $K_{Eu}^{apt-plag}$ value. Rearranging and combining equations of the form of Eq. (15) for apatite and plagioclase, the relationship between fO_2 and $D_{Eu}^{apt-plag}$ can be expressed as:

$$D_{Eu}^{apt-plag} = \frac{\left(K_{Eu}^{apt-plag} \times D_{Eu^{2+}}^{apt} + D_{Eu^{3+}}^{apt} \times (fO_2)^{\frac{1}{4}}\right)}{\left(K_{Eu}^{apt-plag} \times D_{Eu^{2+}}^{plag} + D_{Eu^{3+}}^{plag} \times (fO_2)^{\frac{1}{4}}\right)}, \quad (18)$$

where $D_{Eu^{2+}}^{plag}$ and $D_{Eu^{3+}}^{plag}$ are partition coefficients of Eu^{2+} and Eu^{3+} between plagioclase and silicate melt that can be calculated by predictive models in Sun et al. (2017). By nonlinear least squares regression, we determined the $K_{Eu}^{apt-plag}$ as:

$$K_{Eu}^{apt-plag} = 6.15 \times 10^{-4} \pm 5.71 \times 10^{-5}, \quad (19)$$

which is very close to the value obtained from apatite data (Eq. (16) or plagioclase-melt data (Dygert et al., 2020) alone. Applying this $K_{Eu}^{apt-plag}$ value, we successfully predict almost all experimentally determined D_{Eu} of plagioclase and apatite at the run conditions (T, P, and fO_2; Fig. 6B). After the rearrangement of Eq. (18), we can calculate the fO_2 of the mineral–mineral system by:

$$\log fO_2 = 4 \times log\left(\frac{K_{Eu}^{apt-plag}\left(D_{Eu}^{apt-plag} \times D_{Eu^{2+}}^{plag} - D_{Eu^{2+}}^{apt}\right)}{\left(D_{Eu^{3+}}^{apt} - D_{Eu}^{apt-plag} \times D_{Eu^{3+}}^{plag}\right)}\right), \quad (20)$$

where $D_{Eu}^{apt-plag}$ is the measured Eu distribution between the two phases. The new apatite-plagioclase oxybarometer reveals more variation between fO_2 and $D_{Eu}^{apt-plag}$ than the Eu-in-apatite oxybarometer at all geologically relevant fO_2s, and is more sensitive than the Eu-in-plagioclase oxybarometer in relatively reduced environments (Fig. 7). The Eu in apatite-plagioclase oxybarometer is applicable to natural systems under a wide range of fO_2 conditions.

Because predictive partitioning models for plagioclase and apatite are only sensitive to the composition of the crystalline phase, in order to apply this apatite-plagioclase oxybarometer, one only needs to analyze the major element and Eu concentrations in coexisting apatite and plagioclase that are in equilibrium. After measuring the apatite-plagioclase Eu partition coefficient, Eu^{2+} and Eu^{3+} partition coefficients calculated by models in this study and Sun et al. (2017), one then calculates the fO_2 of the magmatic system using Eq. (20). As an experimental test of the new oxybarometer, we calculated the apatite-plagioclase pair in our experimental product (OHAp-1). The calculated log(fO_2) is −13.9 at 1050 °C, which is consistent with the log(fO_2) value that we determined by the Fe-Pt alloy in a wire sensor in the experiment under the same experimental condition (-14.0; Table 4; Fig. S7).

Although the model is parameterized using mineral-melt partitioning data, lacking any melt composition terms, it can be extrapolated to subsolidus systems. As a preliminary application, we calculated the fO_2 in a coexisting apatite-plagioclase pair from a winonaite Hammadah al Hamra 193 (HaH 193; data from Floss et al., 2007; Floss et al., 2008). We

assume the equilibrium temperature is ~ 1100 ℃ as suggested by two pyroxene thermometry applied to Winona (Benedix et al., 2005; Kretz, 1982), and a pressure of 100 bars. The log(fO_2) we calculate by Eq. (20) is −14.9 at 1100 ℃ (IW-1.6, close to the fO_2 range from IW to 3.0 to IW-2.0 suggested by previous research, e.g., Wadhwa, 2008). As an application to a more oxidized system, we investigated 5 pairs of coexisting apatite-plagioclase from Sept Iles Intrusive Suite (Kieffer et al., 2023). We assume the equilibrium temperature is 1050 ℃ based on the estimated temperature of megacyclic unit I (MCU I) residual liquid after the crystallization of apatite-rich layer (Namur et al., 2011). Assuming a pressure of 100 bars, the calculated log(fO_2) varies from −10.3 to −9.6 (FMQ-0.1 to FMQ + 0.6), in agreement with suggestion of Namur et al. (2010) that most of the Sept Iles layered intrusion crystallized under the fO_2 close to the FMQ buffer. The major and trace element data we used in the calculation are compiled in Table S7. The apatite trace element partition coefficient calculator and Eu in apatite-plagioclase oxybarometer are provided in an Excel spreadsheet in the Supplementary Materials, which also includes all the data we utilized in this study.

4.4. Kinetic fractionation of divalent and trivalent Eu during subsolidus reequilibration and its effect on Eu in apatite-plagioclase oxybarometer

The Eu in apatite-plagioclase oxybarometer that we developed in Section 4.3.4 takes advantage of differences in the partitioning behavior of Eu^{2+} and Eu^{3+} between minerals to quantify fO_2. An important aspect to consider is the response of the oxybarometer to cooling. If a sample is in equilibrium and then quenched or cooling very fast, the fO_2 can be recorded accurately by oxybarometer. However, if the sample cools slowly, experiencing subsolidus reequilibration, then Eu will be redistributed according to the partition coefficients and diffusion rates of Eu^{2+} and Eu^{3+} between apatite and plagioclase. If we do not correctly evaluate the temperature at which the new equilibrium is established, applying the oxybarometer may lead to misleading results. Previous studies suggest the diffusion rate of Eu^{2+} is several orders of magnitude faster than Eu^{3+} in FlAp and plagioclase (e.g., Cherniak and Watson, 1992; Cherniak, 2003; Cherniak, 2010). This difference in diffusion rate has the potential to produce kinetic fractionation, as Eu^{2+} can approach the new equilibrium much faster than Eu^{3+}, and thus affect the prediction of our oxybarometer under disequilibrium conditions. In the following, we apply a forward model to evaluate the effect of kinetic fractionation of Eu on oxybarometric determinations. Due to the lack of data on the diffusion of trace elements in ClAp and the similarity in mineral structures between FlAp and OHAp, the numerical simulations are most relevant to Eu fractionation between FlAp/OHAp and plagioclase.

We made the following simplifying assumptions: (1) Eu^{3+} and Eu^{2+} diffuse through a one-dimensional apatite-plagioclase pair; (2) the system is closed and the fO_2 of the system is maintained two log units lower than IW buffer, thus when the temperature of the system varies, we assume Eu species proportion immediately responds to the change in fO_2 value; (3) the system is only composed of apatite and plagioclase, and the grain size ratio of minerals equals the mass proportions of minerals; (4) flux is conserved at the apatite-plagioclase interface, and the interface always maintains equilibrium partitioning; (5) there is no flux at far side boundary of the minerals; (6) because the Eu^{2+} diffusion in apatite is much faster than Eu^{3+} (e.g., the diffusivities differ by approximately three orders of magnitude at 900 ℃), we assume diffusion of Eu^{2+} in apatite is instantaneous; (7) other coupled redox reactions that could be affected by this temperature change are not considered (e.g., Schreiber, 1986; Schreiber et al., 1987); (8) although the new equilibrium is established at a lower temperature, to test the effect of mistakenly assuming constant temperature, we assume that one ignores the temperature reduction due to cooling and considers that apatite and plagioclase reach equilibrium at the initial temperature, and then use this distribution to calculate the partition coefficients for Eu^{2+} and Eu^{3+}, which leads to discrepancies between the calculation and the actual fO_2. (For comparison, model cases where the correct final temperature is assumed are shown in Fig. S8). The elemental concentrations of apatite and plagioclase used in the modeling are from lunar granulite 79,215 (Treiman et al., 2014). We calculate the Eu^{2+} concentration in the apatite (except for the boundary) by mass balance:

$$C_{apt}^{Subsolidus} = \frac{C_{Bulk}^{Subsolidus}}{\phi_{plag} \times D_i^{plag\text{-}apt} + \phi_{apt}}, \quad (21)$$

where $C_{Bulk}^{Subsolidus}$ is the bulk concentration of element i after temperature variation, ϕ_{plag} and ϕ_{apt} are the mass proportions of the two minerals in the system, which we approximate here by mineral grain size proportions, $D_i^{plag\text{-}apt}$ is the partition coefficient of element i between plagioclase and apatite, $C_{apt}^{Subsolidus}$ is the concentration of element i in apatite at subsolidus temperature.

In a reference model, we assume the apatite (L_{apt} = 100 μm) and plagioclase (L_{plag} = 400 μm) are at first in equilibrium at 1100 ℃, and record the fO_2 of the system at an initial fO_2 (IW-2). Then the temperature of the system instantaneously decreases to 900 ℃. The diffusive concentration profiles are solved numerically using a finite diffusion method and are given in Fig. 8. The modeling method and related equations are described in Yao and Liang (2015) and Zhang (2009). We take the average Eu concentration along the profile as the analyzed mineral Eu concentration and calculated the fO_2 of the system by our Eu in apatite-plagioclase oxybarometer to evaluate the effect produced by subsolidus reequilibration (Fig. 9). We use the mass balance equation and the subsolidus temperature to calculate the Eu^{2+} and Eu^{3+} concentrations in apatite and plagioclase when reequilibration is completed, and we mark the calculated fO_2 at this time as the "apparent ultimate fO_2", which an artifact of mistakenly assuming an elevated (magmatic) temperature rather than a subsolidus temperature (red lines in Fig. 9).

As shown in Fig. 8, the Eu^{2+} between apatite and plagioclase reaches a new equilibrium after ~ 1 million years of diffusive exchange, while the Eu^{3+} takes much longer, especially in plagioclase (characteristic diffusion timescales of Eu^{3+} are ~ 100 Myrs at the simulation temperature). However, because the Eu^{3+} concentration in plagioclase is much lower than in apatite, Eu^{3+} variations in both apatite and plagioclase are limited, which makes the exchange of Eu^{3+} between apatite and plagioclase negligible. This can be further demonstrated by our calculation that after ~ 1 million years, the calculated fO_2 is close to the apparent ultimate fO_2 which is about 0.4 log units more oxidized than IW-2 buffer at 1100℃ (Fig. 9A). In other words, the diffusion of Eu^{2+}, instead of Eu^{3+}, controls the recovered fO_2 variation after the reequilibration relative to a buffer (in addition to the temperature).

In the reference case shown in Fig. 9A, because the fO_2 value at 900 ℃ is ~3.5 log units more reduced than the fO_2 value at 1100 ℃, some Eu^{3+} will convert to Eu^{2+} when temperature suddenly drops to the subsolidus temperature, resulting in an underestimated initial fO_2 value (close to IW-4 at 1100 ℃). However, with the diffusion of Eu, Eu^{2+} will progressively enter apatite from plagioclase, leading to the calculated fO_2 increasing, until Eu^{2+} approaches the new equilibrium condition, which causes the calculated fO_2 to approach the apparent ultimate fO_2. Fig. 9B and 9C show cases where grain size of plagioclase and apatite respectively are varied. The results demonstrate that because the diffusion rate of Eu^{2+} in apatite is rapid, changing the apatite size does not have any obvious effect on reequilibration timescale (Fig. 9B). For plagioclase, however, the one order of magnitude smaller grain produces two orders of magnitude shorter reequilibration time (Fig. 9C). The grain size variation will not produce any change in apparent ultimate fO_2, since the concentration ratio of elements after the subsolidus reequilibration is independent of the mass ratio of minerals.

We subsequently tested the effect of the cooling path by modifying the initial and subsolidus temperatures (Fig. 9D and 9E). We found the initial temperatures have a very limited effect on the reequilibration

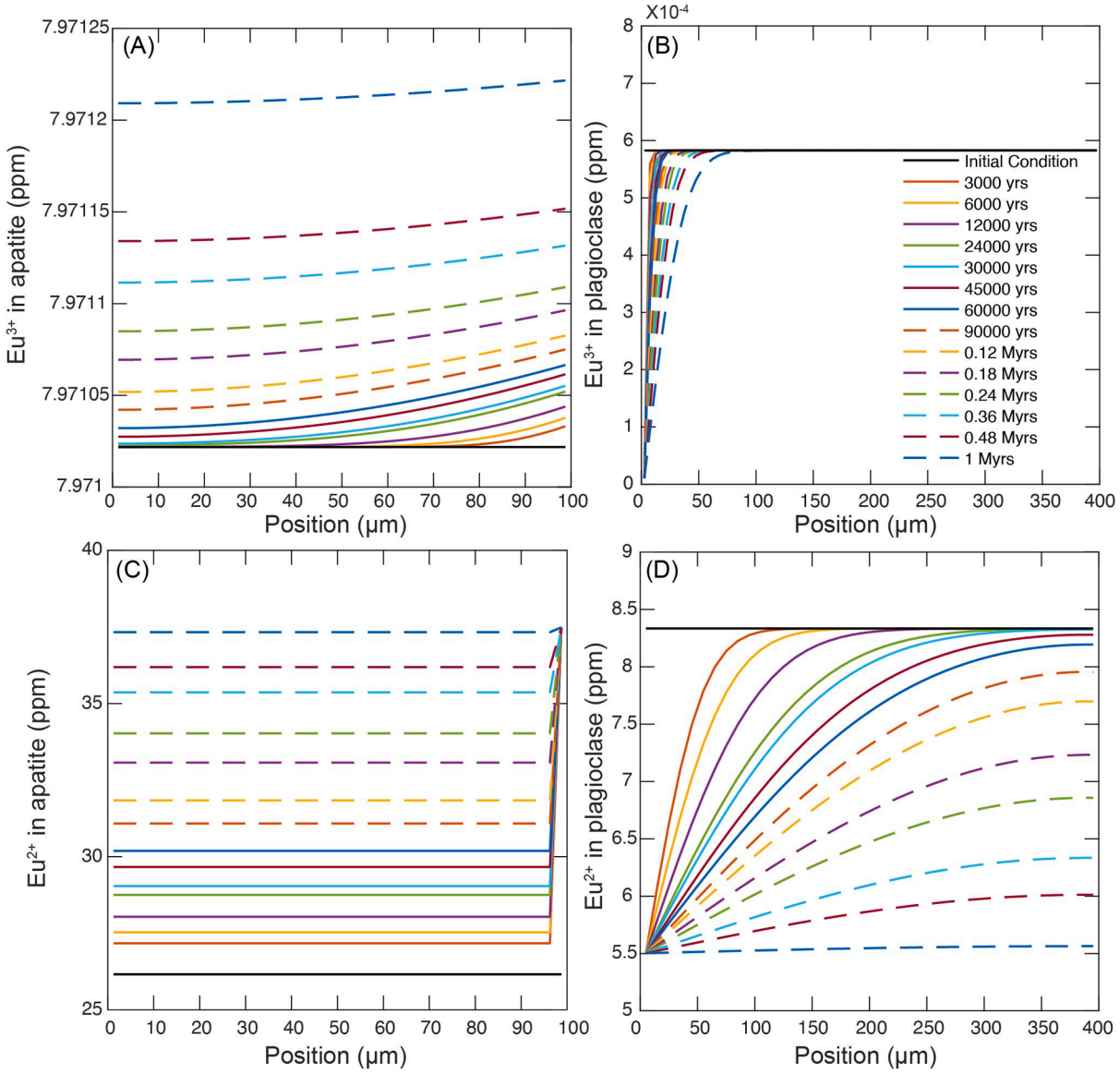

Fig. 8. Diffusion profiles for (**A-B**) Eu^{3+} and (**C-D**) Eu^{2+} between apatite and plagioclase at 14 selected times during subsolidus reequilibration simulations. The apatite (L_{apt} = 100 μm) and plagioclase (L_{plag} = 400 μm) initially are in equilibrium at 1100 ℃, and the system instantaneously cools to 900 ℃ (subsolidus temperature) which triggers the reequilibration.

timescale but can change the apparent ultimate fO_2 since we utilize initial temperature to calculate the predictive partition coefficients of Eu^{2+} and Eu^{3+} (compare Fig. 9A and 9D). As for subsolidus temperatures, 100 ℃ lower subsolidus temperature will generate one order of magnitude longer equilibration timescale, and one log unit further overestimation of fO_2 (compare Fig. 9A and 9E). According to the calculations, regardless of the temperature assumed, the larger the grain size and the higher proportion of plagioclase in the system, the longer the time required to achieve reequilibration. For many geologically-relevant scenarios, plagioclase and apatite will approach Eu^{2+} equilibrium over timescales of millions of years, but subsolidus reequilibration during cooling will induce a deviation of the recovered fO_2 from the actual fO_2 if the new equilibrium temperature is not considered.

Accurately estimating the subsolidus reequilibration temperature is key to avoiding miscalculated fO_2s. If we accurately apply the new equilibrium temperature, the oxybarometer will return the correct fO_2 value after the completion of reequilibration (compare Fig. S8A-S8B to S8C-S8D). Since the diffusivity of Eu^{2+} in plagioclase governs the reequilibration timescale, future research should focus on developing an plagioclase thermometer with closure temperature analogous to Eu^{2+} to help calibrate the divergence from the real fO_2.

5. Implications for the relative volatile budget of lunar magma ocean cumulates

Many estimates of the volatile contents of the interior of the Moon are achieved through two approaches: direct measurements of the compositions of lunar rocks and minerals (e.g., Hui et al., 2013; Treiman et al., 2014), and direct measurements of volcanic glasses (e.g., Albarède et al., 2015; Hauri et al., 2015; Saal et al., 2008) and melt inclusions in returned samples (e.g., Hauri et al., 2011; Ni et al., 2019), both coupled with petrogenetic models. Nominally anhydrous minerals have very low partition coefficients for volatiles as the volatiles can only enter lattice defects (Bell and Rossman, 1992; Libowitzky and Beran, 2006), resulting in increased concentrations of volatiles in LMO residual liquid as well as in late-formed phases that precipitated from the magma ocean (i.e., apatite; McCubbin et al., 2015b). In apatite, because the X-site can accommodate volatile elements, volatile abundances can be directly

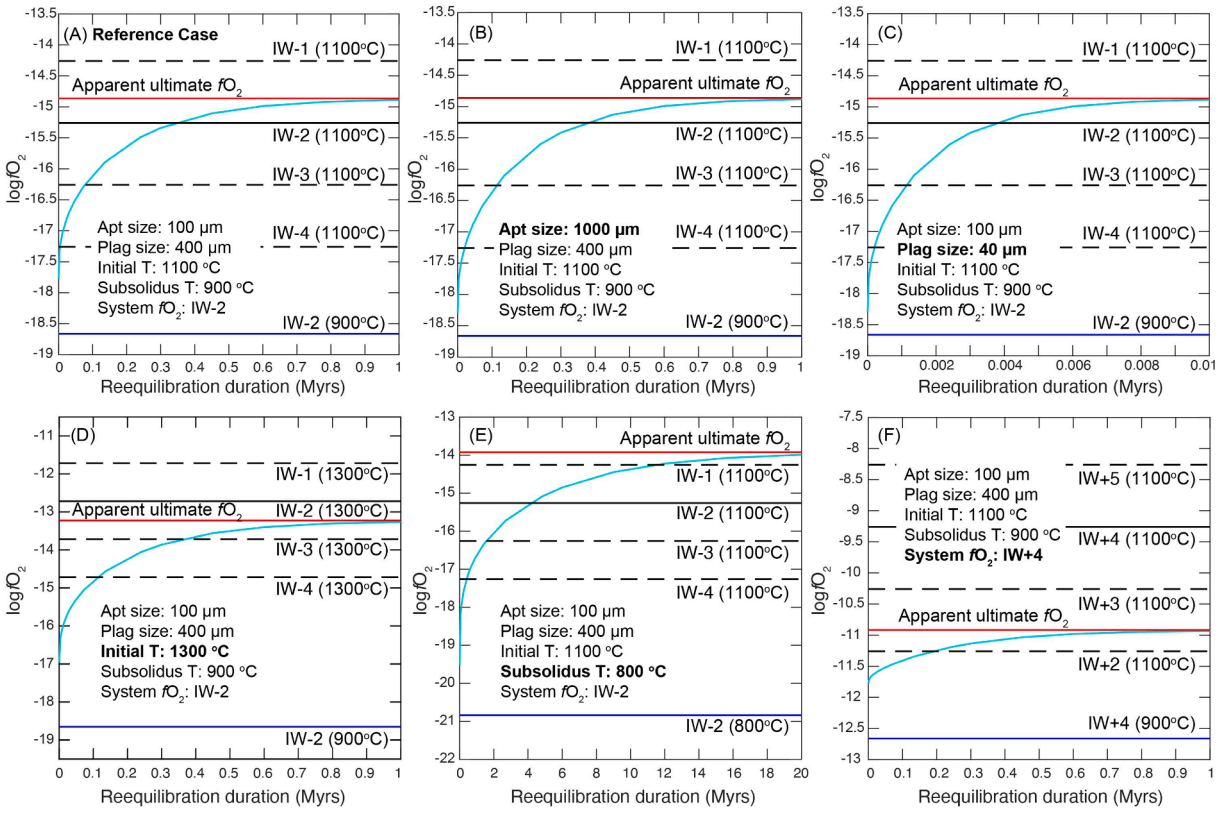

Fig. 9. Figures illustrating the effect of grain size of plagioclase and apatite, initial temperature, subsolidus temperature and fO_2 of the system to our oxybarometer during subsolidus reequilibration. In a reference case (A) we assume the apatite grain is 100 μm, the plagioclase grain is 400 μm, the initial temperature is 1100 °C, the subsolidus temperature is 900 °C, and the fO_2 of the system is IW-2. Then we varied one parameter in each simulation relative to the reference case showing in Fig. 9A to test the following effects: (B) the apatite grain is 1000 μm; (C) the plagioclase grain is 40 μm; (D) the initial temperature is 1300 °C; (E) the subsolidus temperature is 800 °C; and (F) the fO_2 of the system is IW + 4.

measured to characterize a magmatic system. Nonetheless, special care must be taken, as the volatile partition coefficient between apatite and silicate melt vary ($D_F > D_{Cl} > D_{OH}$; McCubbin et al., 2015a); the volatile concentrations in the lunar apatite cannot be directly equated with the volatile concentration in the LMO. In addition, lunar apatites in returned samples may be highly misleading as some might be products of fractional crystallization after apatite saturation, especially for apatites relatively enriched in Cl and OH (Boyce et al., 2014). On the other hand, volatiles are difficult to estimate in volcanic glasses because of the difficulty of quantifying diffusive degassing after eruption (McCubbin et al., 2015b).

We take advantage of our partition coefficient models to provide an indirect method to evaluate the relative volatile contents during the LMO crystallization, circumventing complex secondary effects that plague direct measurements of volatiles in lunar samples. The slope of the REE partition coefficients across the lanthanides is distinct for ClAp compared to OHAp and FlAp. To explore the consequences of potential apatite species on lunar trace element patterns, we use LMO crystallization sequence in Rapp and Draper (2018) to calculate trace element fractionation during LMO solidification, assuming that the apatite reaches saturation at 97 % solidification. The apatite compositions we applied are from two experiments (FlAp-9 and ClAp-1) since our experimental initial composition and fO_2 are highly lunar relevant. We applied our new predictive models to calculate the concentrations of trivalent and divalent elements and Eu in apatite during lunar magma ocean solidification. For other minerals, we use the major element concentrations reported in Rapp and Draper (2018) to calculate their trace element partition coefficients, as described in Ji and Dygert (2023).

First, we test the scenario that partial melting of late-stage LMO cumulates explains the petrogenesis of lunar KREEP basalt. We simplify partial melting as modal fractional melting and apply the equation from Shaw (1970) to calculate the concentration of element i in the incremental liquid:

$$C_L^i = C_o^i \times (1-F)^{\left(\frac{1}{D_{Bulk}^i - 1}\right)}, \quad (22)$$

where C_L^i is the concentration of element i in the incremental liquid, C_o^i is the concentration of element i in the source of the KREEP basalt, F is the degree of melting, and D_{Bulk}^i is the bulk partition coefficient of the KREEP basalt source calculated by the weighted average of partition coefficients between mineral and liquid based on assumed mineral modes. The results show that the compositions of the LMO residual liquid are similar under the assumption that different species of apatite are crystallized, but the compositions of the remelts of late LMO cumulates are very different among the apatite species, especially for light REEs (Fig. 10A). We compare our calculation with KREEP basalts, and observe that the first 5 % of remelts produced when apatites are assumed to be FlAp or OHAp, with a source of 27 % plagioclase, 68 % clinopyroxene, 3 % apatite and 2 % of ilmenite, fit the KREEP basalts very well, including their Eu anomalies. However, in ClAp scenario, because of its lower REE partition coefficients, all the REEs, especially the light REEs, are overestimated for the same source mineralogy (Fig. 10A and 10B). This suggests that the apatite in the late-stage LMO cumulates must be relatively enriched in F^- and OH^- and depleted in Cl^- before partial melting that formed the KREEP basalts.

Based on the higher Mg# of orthopyroxene (Opx) in the Apollo 15 KREEP basalt, previous studies suggested the source of the KREEP basalt should be dominated by early stage LMO crystallized Opx, with

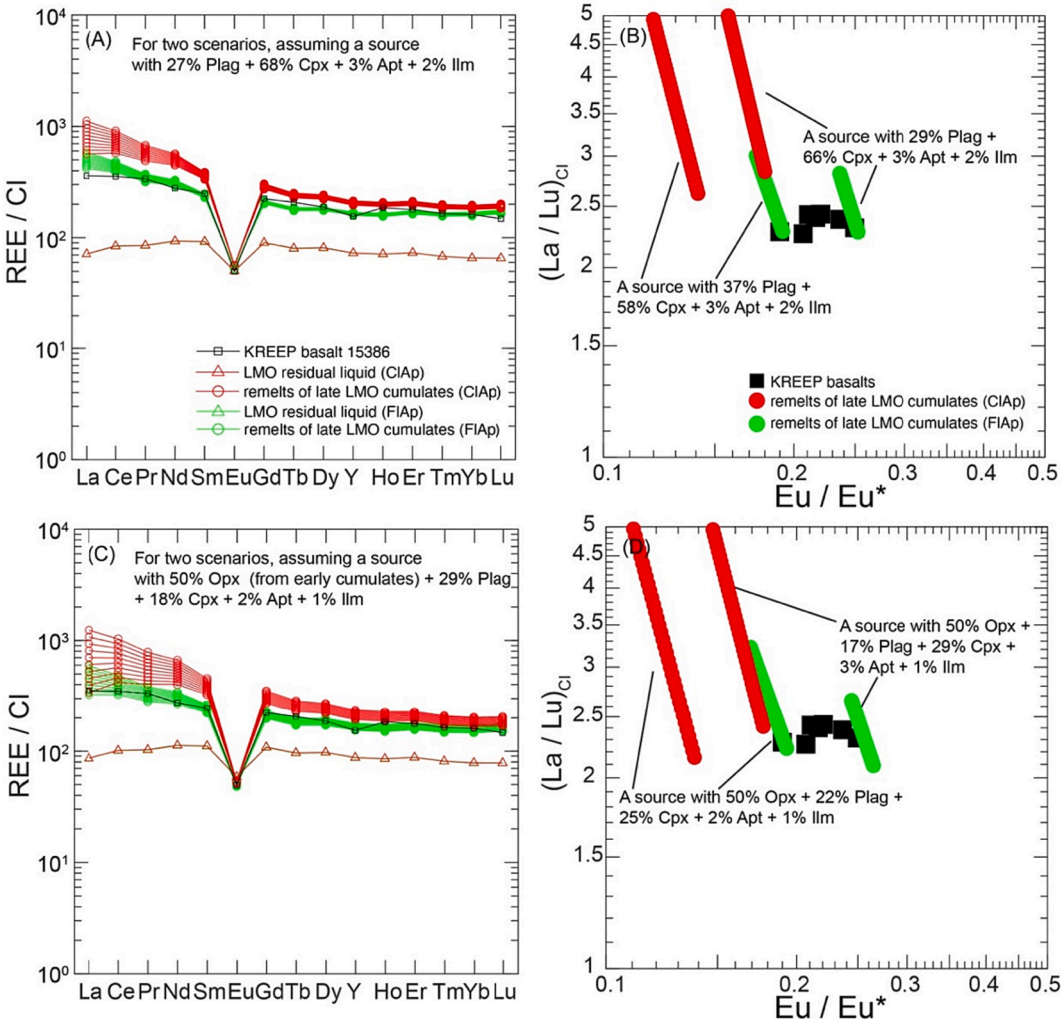

Fig. 10. (A) Chondrite-normalized REE patterns of residual liquids after 98.9 percent solidification of the LMO, and remelts of late LMO cumulates compared to KREEP basalt 15,386 (Neal and Kramer, 2003), and (B) $(La / Lu)_{CI}$ versus Eu / Eu* showing remelts of late LMO cumulates with different source mineral modes and apatite species compared to KREEP basalts (Helmke et al., 1973; Hubbard et al., 1973; McKay et al., 1979; Neal and Kramer, 2003); (C) Chondrite-normalized REE patterns of residual liquids after 90.1 percent solidification of the LMO, and remelts with a source of 50 % late LMO cumulates and 50 % of early LMO crystallized Opx (PCS = 52 %; Rapp and Draper, 2018) compared to KREEP basalt 15386; (D) $(La / Lu)_{CI}$ versus Eu / Eu* showing remelts of late LMO cumulates with different source mineral modes and apatite species compared to KREEP basalts. Chondrite normalization is from Lodders (2021).

plagioclase and variable amounts of phosphates and ilmenite (e.g., Taylor et al., 2012; Cronberger and Neal, 2017). We tested this possibility and assumed that the source is composed of 50 % early LMO crystallized Opx (PCS = 52 %; Rapp and Draper, 2018) and 50 % late LMO cumulates, and compared the remelt compositions of the two endmember scenarios. We found that again, the presence of ClAp in the KREEP basalt source would produce overestimation of light REEs, inconsistent with KREEP basalts (Fig. 10C and 10D).

As apatite is thought to be the major mineral repository of volatile elements among the LMO cumulates, our calculations imply high (F + OH)/Cl in the late-stage LMO, distinct from Cl-rich chondritic precursor materials (Jones et al., 2014; McCubbin et al., 2023). In the early-stage LMO cumulates, due to the significantly lower nominally anhydrous mineral-melt partition coefficients for Cl, Cl will also be depleted compared with the sum of OH and F (Potts et al., 2021). Using analyses of natural materials and assumed partition coefficients, McCubbin et al., (2015b) evaluated the volatile abundance in urKREEP and determined it has 660 ppm F, 1100–1350 ppm Cl and 300–1250 ppm H_2O. If we convert their estimated abundances from weight percent to mol percent, the estimated Cl / (F + OH) = 0.29–0.73, consistent with our prediction.

A caveat in our modeling is the absence of merrillite (or whitlockite) in the late-stage LMO cumulates. Merrillite has been discovered in lunar samples (e.g., Jolliff et al., 2006). As merrillite is anhydrous and should not be interpreted as an indicator of water concentration in a magma (McCubbin et al., 2014), the appearance of merrillite can indicate either phosphorus enrichment or halogen depletion (Douce and Roden, 2006). Given the presence of sufficient halogens (e.g., McCubbin et al., 2015b; Hauri et al., 2015), as well as the anticipated moderate phosphorus content of the LMO (e.g., Charlier et al., 2018; Lin et al., 2017; Rapp and Draper, 2018; Schmidt and Kraettli, 2022), the mineral mode of merrillite should be very limited compared with apatite during LMO solidification. Although there is currently no predictive model for merrillite REE partition coefficients, Jolliff et al. (1993) reported that the REE concentrations of coexisting merrillite and apatite have nearly parallel patterns in lunar samples, but much higher REE concentrations. We tested a scenario where there is a small amount of whitlockite (0.2 to 0.5 wt%) coexisting with apatite (1.0 to 3.0 wt%) during LMO crystallization (Fig. S9). The model shows that the presence of whitlockite will not change the overall REE slope of late-stage LMO remelts or the overestimation of light REE in ClAp scenario (Fig. S9), i.e., our inference that the late LMO was low in Cl relative to F and OH holds.

Here we briefly evaluate the significance of our inference in the

context of previous models for lunar volatile evolution. Depletion of lunar volatiles relative to the Earth has long been noted (e.g., Taylor et al., 2006), but the scale, timing, and duration of the associated degassing processes are controversial. Several studies emphasize the importance of degassing during the giant impact (e.g., Barnes et al., 2016; Gargano et al., 2020). Degassing during the subsequent LMO phase is disputed, with some workers arguing for limited LMO degassing due to the existence of an atmosphere in contact with LMO (e.g., Barnes et al., 2016), and others finding evidence for LMO degassing in the rock record (e.g., Boyce et al., 2015; Ji et al., 2022). If it degasses under low oxygen fugacity, due to differences in diffusion rates, the LMO residual liquid may preferentially lose H (Sharp et al., 2013), resulting in a relatively dry Moon. Subsequently, Cl would combine with metal cations in the magma, such that light ^{35}Cl prefers to evaporate (Sharp et al., 2010), leaving widespread positive δ^{37}Cl values in lunar samples (e.g., Treiman et al., 2014; Wang et al., 2019). Fluorine is the least susceptible to volatilization (Fegley and Schaefer, 2010; Ustunisik et al., 2011; Ustunisik et al., 2015), resulting in relatively less F loss by degassing. Although difficult to quantify, in a giant impact scenario followed by an LMO, differential degassing and the relative loss of Cl and OH may proceed pre- and syn- LMO evolution, consistent with Cl depletion in the late-stage LMO cumulates. Impact-related vapor metasomatism and condensation have been proposed to explain the high δ^{37}Cl values of ancient mare basalt (Barnes et al., 2019), highland breccia (Treiman et al., 2014), and ferroan anorthosites (Gargano et al., 2020). Considering a modest water content in young Chang'e 5 mare basalt (Hu et al., 2021), in a dynamically differentiating Moon (e.g., Hess and Parmentier, 1995), it is possible that the distribution of lunar volatiles was heterogeneous in the lunar interior after the LMO stage, such that multiple reservoirs with distinct volatile concentrations and isotopic compositions developed (e.g., Wang et al., 2019), or perhaps a partly undegassed reservoir exists despite the giant impact (Boyce et al., 2018 and references therein).

6. Conclusions

Accurate knowledge of the high trace element partition coefficients of apatite is essential for successfully modeling the early-stage evolution of Earth and other bodies, and to track the geochemical evolution of evolved magmas. In this study, we measured trace element partition coefficients between three endmember apatites (FlAp, OHAp, and ClAp) and silicate melt at 1050–1100 ℃ at 1 GPa. With the help of these new data, as well as previous experimental work, we developed temperature and composition-dependent predictive partitioning models for divalent and trivalent elements based on the lattice strain model which enable us to calculate the apatite-melt partition coefficients. We observed that the X-site occupancy plays an important role in controlling the substitution mechanisms in the apatite structure and we use apatite major element compositions (as formula units, X_{Ca}, X_{Na}, X_P and X_{Si}) to quantify the influence of the structure on partitioning behavior, after major element substitutions controlled by the anions. We evaluated the impact of fO_2 on Eu anomalies of apatites and conducted three groups of parallel experiments with different capsule types to constrain the fO_2 dependence of Eu partition coefficients between apatite and silicate melt. We developed an fO_2-dependent predictive apatite-melt Eu partitioning model, and Eu in apatite-melt and Eu in apatite-plagioclase oxybarometers, and applied the latter model to calculate the fO_2 of our experiments, the winonaite HaH 193, and Sept Iles layered intrusion. The predictions reproduce their anticipated fO_2s, ranging from about two log units below IW buffer to the FMQ buffer, consistent with previous studies, suggesting the Eu in apatite-plagioclase oxybarometer can be successfully applied to natural systems. We evaluated the impact of kinetic fractionation between trivalent and divalent Eu on our oxybarometer during subsolidus reequilibration, and found the larger the grain size of plagioclase, the slower the system will approach a new equilibrium condition, owing to relatively sluggish diffusion of divalent Eu in plagioclase relative to apatite. Our models emphasize that assumption of an incorrect equilibrium temperature will produce a misestimation of the system fO_2. Finally, we modeled the petrogenesis of lunar KREEP basalt using our predictive partition coefficient models and found that in the late-stage LMO cumulates, Cl is relatively depleted in mole percent compared with the sum of F and OH. Because chondritic precursor materials have subequal F and Cl abundances, a Cl depleted lunar interior suggests that differential degassing occurred before or during the late stages of LMO solidification.

Data availability

Research data has been supplied via a repository: https://doi.org/10.5281/zenodo.10056661.

Declaration of competing interest

The authors declare that they have no known competing financial interests or personal relationships that could have appeared to influence the work reported in this paper.

Acknowledgments

We thank Allan Patchen for his help with electron microprobe analysis, Nathan Miller for his assistance with LA-ICP-MS analysis at the University of Texas, Austin, and Shichun Huang for his help with the dissolution experiments. Thoughtful reviews by two anonymous reviewers and Associate Editor Yuan Li are greatly appreciated. This work was supported by an MSA Student Research Grant to D.J. and NASA Solar System Workings award 80NSSC20K0467 to N.D.

Appendix A. Supplementary material

All data applied in this study and all supporting supplementary figures are presented in the Supplementary Material. We also include the apatite trace element partition coefficients calculator and Eu in apatite-plagioclase oxybarometer in an Excel spreadsheet in the Supplementary Materials.

Supplementary material to this article can be found online at https://doi.org/10.1016/j.gca.2023.11.004.

References

Aigner-Torres, M., Blundy, J., Ulmer, P., Pettke, T., 2007. Laser ablation ICPMS study of trace element partitioning between plagioclase and basaltic melts: an experimental approach. Contrib. Mineral. Petrol. 153, 647–667.

Albarède, F., Albalat, E., Lee, C.T.A., 2015. An intrinsic volatility scale relevant to the Earth and Moon and the status of water in the Moon. Meteoritics & Planetary Science 50 (4), 568–577.

Barnes, J.J., Tartese, R., Anand, M., McCubbin, F.M., Neal, C.R., Franchi, I.A., 2016. Early degassing of lunar urKREEP by crust-breaching impact (s). Earth Planet. Sci. Lett. 447, 84–94.

Barnes, J.J., Franchi, I.A., McCubbin, F.M., Anand, M., 2019. Multiple reservoirs of volatiles in the Moon revealed by the isotopic composition of chlorine in lunar basalts. Geochim. Cosmochim. Acta 266, 144–162.

Bell, D.R., Rossman, G.R., 1992. Water in Earth's mantle: the role of nominally anhydrous minerals. Science 255, 1391–1397.

Benedix, G.K., Lauretta, D.S., McCoy, T.J., 2005. Thermodynamic constraints on the formation conditions of winonaites and silicate-bearing IAB irons. Geochim. Cosmochim. Acta 69, 5123–5131.

Bindeman, I.N., Davis, A.M., 2000. Trace element partitioning between plagioclase and melt: investigation of dopant influence on partition behavior. Geochim. Cosmochim. Acta 64, 2863–2878.

Blundy, J., Wood, B., 1994. Prediction of crystal–melt partition coefficients from elastic moduli. Nature 372, 452–454.

Borisov, S., Klevtsova, R., 1963. The crystal structure of REE-Sr apatite. Zhurnal Strukturnoi Khimii 4, 629–631.

Boyce, J.W., Kanee, S.A., McCubbin, F.M., Barnes, J.J., Bricker, H., Treiman, A.H., 2018. Early loss, fractionation, and redistribution of chlorine in the Moon as revealed by the low-Ti lunar mare basalt suite. Earth Planet. Sci. Lett. 500, 205–214.

Boyce, J., Tomlinson, S., McCubbin, F., Greenwood, J., Treiman, A., 2014. The lunar apatite paradox. Science 344, 400–402.

Boyce, J.W., Treiman, A.H., Guan, Y., Ma, C., Eiler, J.M., Gross, J., Greenwood, J.P., Stolper, E.M., 2015. The chlorine isotope fingerprint of the lunar magma ocean. Sci. Adv. 1, e1500380.

Brice, J., 1975. Some thermodynamic aspects of the growth of strained crystals. J. Cryst. Growth 28, 249–253.

Charlier, B., Grove, T.L., Namur, O., Holtz, F., 2018. Crystallization of the lunar magma ocean and the primordial mantle-crust differentiation of the Moon. Geochim. Cosmochim. Acta 234, 50–69.

Chen, Y., Li, H., Sun, W., Ireland, T., Tian, X., Hu, Y., Yang, W., Chen, C., Xu, D., 2016. Generation of Late Mesozoic Qianlishan A2-type granite in Nanling Range, South China: implications for Shizhuyuan W-Sn mineralization and tectonic evolution. Lithos 266, 435–452.

Chen, N., Pan, Y., Weil, J.A., Nilges, M.J., 2002. Electron paramagnetic resonance spectroscopic study of synthetic fluorapatite: Part II. Gd3+ at the Ca1 site, with a neighboring Ca2 vacancy. Am. Mineral. 87, 47–55.

Cherniak, D., 2000. Rare earth element diffusion in apatite. Geochim. Cosmochim. Acta 64, 3871–3885.

Cherniak, D., 2003. REE diffusion in feldspar. Chem. Geol. 193, 25–41.

Cherniak, D., 2010. Diffusion in accessory minerals: zircon, titanite, apatite, monazite and xenotime. Rev. Mineral. Geochem. 72, 827–869.

Cherniak, D., Ryerson, F., 1993. A study of strontium diffusion in apatite using Rutherford backscattering spectroscopy and ion implantation. Geochim. Cosmochim. Acta 57, 4653–4662.

Cherniak, D., Watson, E., 1992. A study of strontium diffusion in K-feldspar, Na-K feldspar and anorthite using Rutherford Backscattering Spectroscopy. Earth Planet. Sci. Lett. 113, 411–425.

Cockbain, A., Smith, G., 1967. Alkaline-earth-rare-earth silicate and germanate apatites. Mineralogical Magazine and Journal of the Mineralogical Society 36, 411–421.

Cronberger, K., Neal, C.R., 2017. KREEP basalt petrogenesis: Insights from 15434, 181. Meteorit. Planet. Sci. 52, 827–841.

Douce, A.E.P., Roden, M., 2006. Apatite as a probe of halogen and water fugacities in the terrestrial planets. Geochim. Cosmochim. Acta 70, 3173–3196.

Drake, M.J., 1975. The oxidation state of europium as an indicator of oxygen fugacity. Geochim. Cosmochim. Acta 39, 55–64.

Dygert, N., Liang, Y., Sun, C., Hess, P., 2014. An experimental study of trace element partitioning between augite and Fe-rich basalts. Geochim. Cosmochim. Acta 132, 170–186.

Dygert, N., Draper, D.S., Rapp, J.F., Lapen, T.J., Fagan, A.L., Neal, C.R., 2020. Experimental determinations of trace element partitioning between plagioclase, pigeonite, olivine, and lunar basaltic melts and an fO_2 dependent model for plagioclase-melt Eu partitioning. Geochim. Cosmochim. Acta 279, 258–280.

Ertel, W., O'Neill, H.S.C., Sylvester, P.J., Dingwell, D., Spettel, B., 2001. The solubility of rhenium in silicate melts: Implications for the geochemical properties of rhenium at high temperatures. Geochim. Cosmochim. Acta 65, 2161–2170.

Fabbrizio, A., Schmidt, M.W., Petrelli, M., 2021. Effect of fO2 on Eu partitioning between clinopyroxene, orthopyroxene and basaltic melt: Development of a Eu3+/Eu2+ oxybarometer. Chem. Geol. 559, 119967.

Fegley, B., Schaefer, L., 2010. Cosmochemistry. Springer Berlin Heidelberg, Berlin, Heidelberg, pp. 347–377.

Fleet, M.E., Liu, X., Pan, Y., 2000a. Rare-earth elements in chlorapatite [Ca10(PO4) 6Cl2]: Uptake, site preference, and degradation of monoclinic structure. Am. Mineral. 85, 1437–1446.

Fleet, M.E., Liu, X., Pan, Y., 2000b. Site preference of rare earth elements in hydroxyapatite [Ca10(PO4)6(OH)2]. J. Solid. State. Chem. 149, 391–398.

Fleet, M.E., Pan, Y., 1997. Site preference of rare earth elements in fluorapatite: Binary (LREE+ HREE)-substituted crystals. Am. Mineral. 82, 870–877.

Floss, C., Jolliff, B.L., Benedix, G.K., Stadermann, F.J., Reid, J., 2007. Hammadah al Hamra 193: The first amphibole-bearing winonaite. Am. Mineral. 92, 460–467.

Floss, C., Crozaz, G., Jolliff, B., Benedix, G., Colton, S., 2008. Evolution of the winonaite parent body: Clues from silicate mineral trace element distributions. Meteorit. Planet. Sci. 43, 657–674.

Gargano, A., Sharp, Z., Shearer, C., Simon, J.I., Halliday, A., Buckley, W., 2020. The Cl isotope composition and halogen contents of Apollo-return samples. Proc. Natl. Acad. Sci. u.s.a. 117, 23418–23425.

Gromet, L.P., Silver, L.T., 1983. Rare earth element distributions among minerals in a granodiorite and their petrogenetic implications. Geochim. Cosmochim. Acta 47, 925–939.

Hauri, E.H., Weinreich, T., Saal, A.E., Rutherford, M.C., Van Orman, J.A., 2011. High pre-eruptive water contents preserved in lunar melt inclusions. Science 333, 213–215.

Hauri, E.H., Saal, A.E., Rutherford, M.J., Van Orman, J.A., 2015. Water in the Moon's interior: Truth and consequences. Earth Planet. Sci. Lett. 409, 252–264.

Helmke, P.A., Blanchard, D.P., Haskin, L.A., Telander, K., Weiss, C., Jacobs, J.W., 1973. Major and trace elements in igneous rocks from Apollo 15. The Moon 8, 129–148.

Hess, P.C., Parmentier, E., 1995. A model for the thermal and chemical evolution of the Moon's interior: Implications for the onset of mare volcanism. Earth and Planetary Science Letters 134 (3–4), 501–514.

Holzheid, A., O'Neill, H.S.C., 1995. The Cr-Cr_2O_3 oxygen buffer and the free energy of formation of Cr_2O_3 from high-temperature electrochemical measurements. Geochim. Cosmochim. Acta 59, 475–479.

Hu, S., He, H., Ji, J., Lin, Y., Hui, H., Anand, M., Tartèse, R., Yan, Y., Hao, J., Li, R., 2021. A dry lunar mantle reservoir for young mare basalts of Chang'e-5. Nature 600, 49–53.

Hubbard, N.J., Rhodes, J.M., Gast, P.W., Bansal, B., Shih, C.-Y., Wiesmann, H. and Nyquist, L.E. 1973. Lunar rock types: The role of plagioclase in non-mare and highland rock types, Lunar and Planetary Science Conference Proceedings, p. 1297.

Hughes, J.M., Cameron, M., Crowley, K.D., 1991. Ordering of divalent cations in the apatite structure: Crystal structure refinements of natural Mn-and Sr-bearing apatite. Am. Mineral. 76, 1857–1862.

Hui, H., Peslier, A.H., Zhang, Y., Neal, C.R., 2013. Water in lunar anorthosites and evidence for a wet early Moon. Nat. Geosci. 6, 177–180.

Ito, J., 1968. Silicate apatites and oxyapatites. Am. Mineral. 53, 890–907.

Ji, D., Dygert, N., 2023. Trace element evidence for serial processing of the lunar flotation crust and a depleted bulk Moon. Earth Planet. Sci. Lett. 602, 117958.

Ji, J., He, H., Hu, S., Lin, Y., Hui, H., Hao, J., Li, R., Yang, W., Yan, Y., Tian, H., 2022. Magmatic chlorine isotope fractionation recorded in apatite from Chang'e-5 basalts. Earth Planet. Sci. Lett. 591, 117636.

Jolliff, B.L., Haskin, L.A., Colson, R.O., Wadhwa, M., 1993. Partitioning in REE-saturating minerals: Theory, experiment, and modelling of whitlockite, apatite, and evolution of lunar residual magmas. Geochim. Cosmochim. Acta 57, 4069–4094.

Jolliff, B.L., Hughes, J.M., Freeman, J.J., Zeigler, R.A., 2006. Crystal chemistry of lunar merrillite and comparison to other meteoritic and planetary suites of whitlockite and merrillite. Am. Mineral. 91, 1583–1595.

Jones, R.H., McCubbin, F.M., Dreeland, L., Guan, Y., Burger, P.V., Shearer, C.K., 2014. Phosphate minerals in LL chondrites: A record of the action of fluids during metamorphism on ordinary chondrite parent bodies. Geochim. Cosmochim. Acta 132, 120–140.

Kessel, R., Beckett, J.R., Stolper, E.M., 2001. Thermodynamic properties of the Pt-Fe system. Am. Mineral. 86, 1003–1014.

Ketcham, R.A., 2015. Calculation of stoichiometry from EMP data for apatite and other phases with mixing on monovalent anion sites. Am. Mineral. 100, 1620–1623.

Kieffer, M.A., Dare, S.A., Namur, O., 2023. The use of trace elements in apatite to trace differentiation of a ferrobasaltic melt in the Sept-Iles Intrusive Suite, Quebec, Canada: Implications for provenance discrimination. Geochim. Cosmochim. Acta 342, 169–197.

Klement, R., Haselbeck, H., 1965. Apatite und Wagnerite zweiwertiger Metalle. Zeitschrift Für Anorganische Und Allgemeine Chemie 336, 113–128.

Kretz, R., 1982. Transfer and exchange equilibria in a portion of the pyroxene quadrilateral as deduced from natural and experimental data. Geochim. Cosmochim. Acta 46, 411–421.

Li, W., Costa, F., Oppenheimer, C., Nagashima, K., 2023. Volatile and trace element partitioning between apatite and alkaline melts. Contrib. Mineral. Petrol. 178, 9.

Li, H., Hermann, J., 2017. The effect of fluorine and chlorine on trace element partitioning between apatite and sediment melt at subduction zone conditions. Chem. Geol. 473, 55–73.

Libowitzky, E., Beran, A., 2006. The structure of hydrous species in nominally anhydrous minerals: Information from polarized IR spectroscopy. Rev. Mineral. Geochem. 62, 29–52.

Lin, Y., Tronche, E.J., Steenstra, E.S., Van Westrenen, W., 2017. Experimental constraints on the solidification of a nominally dry lunar magma ocean. Earth Planet. Sci. Lett. 471, 104–116.

Lodders, K., 2021. Relative atomic solar system abundances, mass fractions, and atomic masses of the elements and their isotopes, composition of the solar photosphere, and compositions of the major chondritic meteorite groups. Space Sci. Rev. 217, 1–33.

Mallmann, G., Burnham, A.D., Fonseca, R.O., 2021. Mineral-Melt Partitioning of Redox-Sensitive Elements. Magma Redox Geochemistry 345–367.

McCanta, M.C., Elkins-Tanton, L., Rutherford, M.J., 2009. Expanding the application of the Eu-oxybarometer to the lherzolitic shergottites and nakhlites: Implications for the oxidation state heterogeneity of the Martian interior. Meteorit. Planet. Sci. 44, 725–745.

McCubbin, F.M., Jones, R.H., 2015. Extraterrestrial apatite: Planetary geochemistry to astrobiology. Elements 11, 183–188.

McCubbin, F.M., Shearer, C.K., Burger, P.V., Hauri, E.H., Wang, J., Elardo, S.M., Papike, J.J., 2014. Volatile abundances of coexisting merrillite and apatite in the martian meteorite Shergotty: Implications for merrillite in hydrous magmas. Am. Mineral. 99, 1347–1354.

McCubbin, F.M., Vander Kaaden, K.E., Tartèse, R., Boyce, J.W., Mikhail, S., Whitson, E. S., Bell, A.S., Anand, M., Franchi, I.A., Wang, J., 2015a. Experimental investigation of F, Cl, and OH partitioning between apatite and Fe-rich basaltic melt at 1.0–1.2 GPa and 950–1000 °C. Am. Mineral. 100, 1790–1802.

McCubbin, F.M., Vander Kaaden, K.E., Tartèse, R., Klima, R.L., Liu, Y., Mortimer, J., Barnes, J.J., Shearer, C.K., Treiman, A.H., Lawrence, D.J., 2015b. Magmatic volatiles (H, C, N, F, S, Cl) in the lunar mantle, crust, and regolith: Abundances, distributions, processes, and reservoirs. Am. Mineral. 100, 1668–1707.

McCubbin, F.M., Lewis, J.A., Barnes, J.J., Boyce, J.W., Gross, J., McCanta, M.C., Srinivasan, P., Anzures, B.A., Lunning, N.G., Elardo, S.M., Keller, L.P., Prissel, T.C., Agee, C.B., 2023. On the origin of fluorine-poor apatite in chondrite parent bodies. Am. Mineral. 108, 1185–1200.

McKay, G., Wiesmann, H., Bansal, B., Shih, C.-Y., 1979. Petrology, chemistry, and chronology of Apollo 14 KREEP basalts. Lunar and Planetary Science Conference Proceedings 181–205.

McKay, G., Le, L., Wagstaff, J., Crozaz, G., 1994. Experimental partitioning of rare earth elements and strontium: Constraints on petrogenesis and redox conditions during crystallization of Antarctic angrite Lewis Cliff 86010. Geochim. Cosmochim. Acta 58, 2911–2919.

Médard, E., McCammon, C.A., Barr, J.A., Grove, T.L., 2008. Oxygen fugacity, temperature reproducibility, and H2O contents of nominally anhydrous piston-cylinder experiments using graphite capsules. Am. Mineral. 93, 1838–1844.

Namur, O., Charlier, B., Toplis, M.J., Higgins, M.D., Liégeois, J.-P., Vander Auwera, J., 2010. Crystallization sequence and magma chamber processes in the ferrobasaltic Sept Iles layered intrusion. Canada. J. Petrol. 51, 1203–1236.

Namur, O., Charlier, B., Toplis, M.J., Higgins, M.D., Hounsell, V., Liégeois, J.-P., Vander Auwera, J., 2011. Differentiation of tholeiitic basalt to A-type granite in the Sept Iles layered intrusion. Canada. J. Petrol. 52, 487–539.

Neal, C. and Kramer, G. 2003. The composition of KREEP: A detailed study of KREEP basalt 15386, Lunar and Planetary Science conference, p. 2023.

Ni, P., Zhang, Y., Chen, S., Gagnon, J., 2019. A melt inclusion study on volatile abundances in the lunar mantle. Geochimica Et Cosmochimica Acta 249, 17–41.

Onuma, N., Higuchi, H., Wakita, H., Nagasawa, H., 1968. Trace element partition between two pyroxenes and the host lava. Earth Planet. Sci. Lett. 5, 47–51.

Pan, Y., Fleet, M.E., 2002. Compositions of the apatite-group minerals: substitution mechanisms and controlling factors. Rev. Mineral. Geochem. 48, 13–49.

Potts, N.J., Barnes, J.J., Tartèse, R., Franchi, I.A., Anand, M., 2018. Chlorine isotopic compositions of apatite in Apollo 14 rocks: Evidence for widespread vapor-phase metasomatism on the lunar nearside~ 4 billion years ago. Geochim. Cosmochim. Acta 230, 46–59.

Potts, N.J., Bromiley, G.D., Brooker, R.A., 2021. An experimental investigation of F, Cl and H2O mineral-melt partitioning in a reduced, model lunar system. Geochim. Cosmochim. Acta 294, 232–254.

Pownceby, M.I., O'Neill, H.S.C., 1994. Thermodynamic data from redox reactions at high temperatures. IV. Calibration of the Re-ReO2 oxygen buffer from EMF and NiO+ Ni-Pd redox sensor measurements. Contrib. Mineral. Petrol. 118, 130–137.

Prowatke, S., Klemme, S., 2006. Trace element partitioning between apatite and silicate melts. Geochim. Cosmochim. Acta 70, 4513–4527.

Rapp, J.F., Draper, D.S., 2018. Fractional crystallization of the lunar magma ocean: Updating the dominant paradigm. Meteorit. Planet. Sci. 53, 1452–1455.

Saal, A.E., Hauri, E.H., Cascio, M.L., Van Orman, J.A., Rutherford, M.C., Cooper, R.F., 2008. Volatile content of lunar volcanic glasses and the presence of water in the Moon's interior. Nature 454 (7201), 192–195.

Schmidt, M.W. and Kraettli, G. 2022. Experimental crystallization of the lunar magma ocean, initial selenotherm and density stratification, and implications for crust formation, overturn and the bulk silicate Moon composition. J. Geophys. Res. Planets e2022JE007187.

Schreiber, H.D., 1986. Redox processes in glass-forming melts. Journal of Non-Crystalline Solids 84 (1–3), 129–141.

Schreiber, H.D., Merkel Jr, R.C., Schreiber, V.L., Balazs, G.B., 1987. Mutual interactions of redox couples via electron exchange in silicate melts: models for geochemical melt systems. Journal of Geophysical Research: Solid Earth 92 (B9), 9233–9245.

Shannon, R.D., 1976. Revised effective ionic radii and systematic studies of interatomic distances in halides and chalcogenides. Acta Crystallographica Section a: Crystal Physics, Diffraction, Theoretical and General Crystallography 32, 751–767.

Sharp, Z.D., McCubbin, F.M., Shearer, C.K., 2013. A hydrogen-based oxidation mechanism relevant to planetary formation. Earth Planet. Sci. Lett. 380, 88–97.

Sharp, Z., Shearer, C., McKeegan, K., Barnes, J., Wang, Y., 2010. The chlorine isotope composition of the Moon and implications for an anhydrous mantle. Science 329, 1050–1053.

Shaw, D.M., 1970. Trace element fractionation during anatexis. Geochim. Cosmochim. Acta 34, 237–243.

Shervais, J.W., Taylor, L.A., Laul, J., Smith, M., 1984. Pristine highland clasts in consortium breccia 14305: Petrology and geochemistry. J. Geophys. Res. Solid Earth 89, C25–C40.

Stepanov, A.S., Zhukova, I.A., Jiang, S.-Y., 2023. Experimental constraints on miscibility gap between apatite and britholite and REE partitioning in an alkaline melt. Am. Mineral. 108, 1043–1052.

Sudarsanan, K., Young, R., 1980. Structure of partially substituted chlorapatite (Ca2Sr)5 (PO4)3Cl. Acta Crystallographica Section b: Structural Crystallography and Crystal Chemistry 36, 1525–1530.

Sun, C.G., Graff, M., Liang, Y., 2017. Trace element partitioning between plagioclase and silicate melt: The importance of temperature and plagioclase composition, with implications for terrestrial and lunar magmatism. Geochim. Cosmochim. Acta 206, 273–295.

Sun, C., Liang, Y., 2012. Distribution of REE between clinopyroxene and basaltic melt along a mantle adiabat: effects of major element composition, water, and temperature. Contrib. Mineral. Petrol. 163, 807–823.

Tailby, N.D., Trail, D., Watson, B., Lanzirotti, A., Newville, M., Wang, Y., 2023. Eu speciation in apatite at 1 bar: An experimental study of valence-state partitioning by XANES, lattice strain, and Eu/Eu* in basaltic systems. Am. Mineral. 108, 789–813.

Tartèse, R., Anand, M., McCubbin, F.M., Elardo, S.M., Shearer, C.K., Franchi, I.A., 2014. Apatites in lunar KREEP basalts: The missing link to understanding the H isotope systematics of the Moon. Geology 42, 363–366.

Taylor, G.J., Martel, L.M., Spudis, P.D., 2012. The Hadley-Apennine KREEP basalt igneous province. Meteorit. Planet. Sci. 47, 861–879.

Taylor, S.R., Pieters, C.M., MacPherson, G.J., 2006. Earth-Moon system, planetary science, and lessons learned. Rev. Mineral. Geochem. 60, 657–704.

Tepley III, F.J., Lundstrom, C.C., McDonough, W.F., Thompson, A., 2010. Trace element partitioning between high-An plagioclase and basaltic to basaltic andesite melt at 1 atmosphere pressure. Lithos 118, 82–94.

Treiman, A.H., Boyce, J.W., Gross, J., Guan, Y., Eiler, J.M., Stolper, E.M., 2014. Phosphate-halogen metasomatism of lunar granulite 79215: Impact-induced fractionation of volatiles and incompatible elements. Am. Mineral. 99, 1860–1870.

Urusov, V.S., Khudolozhkin, V.O., 1974. An energy analysis of cation ordering in apatite. Geochem. Int. 11, 1048–1053.

Ustunisik, G., Nekvasil, H., Lindsley, D., 2011. Differential degassing of H2O, Cl, F, and S: Potential effects on lunar apatite. Am. Mineral. 96, 1650–1653.

Ustunisik, G., Nekvasil, H., Lindsley, D.H., McCubbin, F.M., 2015. Degassing pathways of Cl-, F-, H-, and S-bearing magmas near the lunar surface: Implications for the composition and Cl isotopic values of lunar apatite. Am. Mineral. 100, 1717–1727.

Wadhwa, M., 2001. Redox state of Mars' upper mantle and crust from Eu anomalies in shergottite pyroxenes. Science 291, 1527–1530.

Wadhwa, M., 2008. Redox conditions on small bodies, the Moon and Mars. Rev. Mineral. Geochem. 68, 493–510.

Wang, Y., Hsu, W., Guan, Y., 2019. An extremely heavy chlorine reservoir in the Moon: Insights from the apatite in lunar meteorites. Sci. Rep. 9, 1–8.

Watson, E.B., Green, T.H., 1981. Apatite/liquid partition coefficients for the rare earth elements and strontium. Earth Planet. Sci. Lett. 56, 405–421.

Wood, B.J., Blundy, J.D., 1997. A predictive model for rare earth element partitioning between clinopyroxene and anhydrous silicate melt. Contrib. Mineral. Petrol. 129, 166–181.

Yao, L., Liang, Y., 2015. Closure temperature in cooling bi-mineralic systems: I. Definition and with application to REE-in-two-pyroxene thermometer. Geochim. Cosmochim. Acta 162, 137–150.

Yao, L.J., Sun, C.G., Liang, Y., 2012. A parameterized model for REE distribution between low-Ca pyroxene and basaltic melts with applications to REE partitioning in low-Ca pyroxene along a mantle adiabat and during pyroxenite-derived melt and peridotite interaction. Contrib. Mineral. Petrol. 164, 261–280.

Zhang, Y., 2009. Geochemical kinetics. Princeton University Press.